

DEVELOPMENT OF D -TYPE FIBER OPTIC SENSORS FOR DETECTION OF
REFRACTIVE INDEX VARIATION IN EVANESCENT WAVE FIELD

A THESIS SUBMITTED TO
THE GRADUATE SCHOOL OF NATURAL AND APPLIED SCIENCES
OF
MIDDLE EAST TECHNICAL UNIVERSITY

BY
BURCU GÜLERYÜZ

IN PARTIAL FULFILLMENT OF THE REQUIREMENTS
FOR
THE DEGREE OF MASTER OF SCIENCE
IN
METALLURGICAL AND MATERIALS ENGINEERING

SEPTEMBER 2014

Approval of the thesis:

**DEVELOPMENT OF D -TYPE FIBER OPTIC SENSORS FOR DETECTION
OF REFRACTIVE INDEX VARIATION**

submitted by **BURCU GÜLERYÜZ** in partial fulfillment of the requirements for the degree of **Master of Science in Metallurgical and Materials Engineering Department, Middle East Technical University** by,

Prof. Dr. Canan Özgen
Dean, Graduate School of **Natural and Applied Sciences**

Prof. Dr. Hakan C. Gür
Head of Department, **Metallurgical and Materials Engineering**

Assoc. Prof. Dr. Caner Durucan
Supervisor, **Metallurgical and Materials Engineering Dept., METU**

Dr. Mustafa M. Aslan
Co-Supervisor, **Materials Institute, TÜBİTAK - MAM**

Examining Committee Members:

Prof. Dr. M. Kadri Aydınol
Metallurgical and Materials Engineering Dept., METU

Assoc. Dr. Caner Durucan
Metallurgical and Materials Engineering Dept., METU

Assist. Prof. Dr. Y. Eren Kalay
Metallurgical and Materials Engineering Dept., METU

Assist. Prof. Dr. Mert Efe
Metallurgical and Materials Engineering Dept., METU

Dr. Mustafa M. Aslan
Materials Institute, TÜBİTAK - MAM

Date:01.09.2014

I hereby declare that all information in this document has been obtained and presented in accordance with academic rules and ethical conduct. I also declare that, as required by these rules and conduct, I have fully cited and referenced all material and results that are not original to this work.

Name, Last name: Burcu GÜLERYÜZ

Signature :

ABSTRACT

DEVELOPMENT OF D -TYPE FIBER OPTIC SENSORS FOR DETECTION OF REFRACTIVE INDEX VARIATION IN EVANESCENT WAVE FIELD

Gülyüz, Burcu

M.S., Department of Metallurgical and Materials Engineering

Supervisor: Assoc. Prof. Dr. Caner Durucan

Co-Supervisor: Dr. Mustafa M. Aslan

September 2014, 91 pages

The purpose of this study is to design, construct, develop and test D-type multimode fiber optic (F/O) sensors based on evanescent wave field sensing. A comprehensive work has been performed both theoretically and experimentally using a geometrical modification approach to improve the sensors response in different manners for detecting the refractive index (RI) variations and bio-molecular interactions in aqueous environment. In this study, the D-type F/O sensors performance was improved utilizing optical waveguide (OWG) and surface plasmon resonance (SPR) modes in evanescent wave field. Development steps of sensors are; fabrication and characterization of silicon V channels (supporting elements), the F/O cable preparation, adhesion, mechanical lapping and polishing, and assembling the Field Assembly Connectors (FC connectors). These steps are explained in detail and sensor performances are demonstrated for RI changes between 1.33 and 1.47. The highest sensitivity is found to be 2×10^5 refractive index unit (RIU) for the zone of 1.44 and 1.46 RIU. In addition, thin gold film is deposited on the D-type F/O sensors to excite surface plasmon (SP) mode. It is shown that the SP mode can amplify the sensors sensitivity between the 1.33 and 1.44 RIU being known as the dynamic range to monitor the bio-molecular interactions. Furthermore, in order to tune thin gold

film thickness and roughness for a better sensor response, a novel surface modification approach is introduced with plasma etching process.

Keywords: D-Type Fiber Optic Sensors, Surface Plasmon, Optical Waveguide, Evanescent Field, Refractive Index.

ÖZ

EVANESCENT DALGA ALANI İÇERİSİNDE KIRILMA İNDİSİ DEĞİŞİMİNİN ÖLÇÜMÜ İÇİN D-TİPİ FİBER OPTİK ALGILAYICILARIN GELİŞTİRİLMESİ

Gülyüz, Burcu
Yüksek Lisans, Metalürji ve Malzeme Mühendisliği Bölümü
Tez Yöneticisi: Doç. Dr. Caner Durucan
Ortak Tez Yöneticisi: Dr. Mustafa M. Aslan

Eylül 2014, 91 sayfa

Bu çalışmanın amacı evanescent dalga alanını algılayabilen D-tipi çok-modlu fiber optik (F/O) sensörlerinin tasarlanması, üretilmesi, geliştirilmesi ve test edilmesi üzerinedir. Teorik ve deneysel olarak değişik geometrik modifikasyon yaklaşımları kullanılarak sensörün sıvı ortamlardaki kırılma indisi değişimlerine ve biyomoleküler etkileşimlerin incelenmesi konusunda kapsamlı bir çalışma yapıldı. Bu çalışmada, D-tipi F/O sensörlerin performansı evanescent dalga bölgesinde açığa çıkartılabilen yüzey plazmonu ve dalga kılavuzu modları ile güçlendirildi. D-tipi F/O sensörlerin üretilmesi ve geliştirilmesi için izlenen basamaklar şunlardır: Silikon V kanalların (destek elemanlarının) üretilmesi ve karakterizasyonu, F/O kabloların hazırlanması, yapıştırılması, parlatılması ve FC bağlantı elemanlarının birleştirilmesidir. Bu basamaklar detaylı olarak açıklanmış ve üretilen F/O sensörlerin hassasiyetleri 1.33 ve 1.47 kırılma indisi değişimleri için hesaplanmıştır. En yüksek hassasiyet 1.44 - 1.46 kırılma indisi bölgesinde 2×10^5 kırılma indisi birimi (RIU) olarak bulunmuştur. D-tipi F/O sensörlerin üzeri ince bir altın film ile kaplanarak yüzey plazmon (SPR) modu tetiklenmiştir. Aslında SPR modu sensörlerin hassasiyetini biyo-moleküler etkileşim ölçümlerinin dinamik bölgesi olarak bilinen 1.33 ve 1.44 RIU kırılma indisi aralığında güçlendirebilir. Buna ilaveten ince altın filmin

kalınlıđını ve pürüzlülüđünü ayarlayabilmek için plazma aşındırma yöntemi uygulanmıřtır.

Anahtar Kelimeler: D-Tipi Fiber Optik Sensör, Yüzey Plazmonu,Optik Dalga kılavuzu, Evanescent Alanı.

To My Dear Family

ACKNOWLEDGEMENTS

I would like to thank the following people and organizations that have been essential to the completion of my graduate studies and research.

I would like to express my sincere appreciation and gratitude to my research advisors; Mustafa M. Aslan and Caner Durucan for patiently sharing their extensive wisdom, their kind and endless support, continuous guidance and motivation throughout this thesis study. Your support, patience and persistence have helped me to improve both my understanding and experimental application of optics and materials.

I must express my special thanks to my co-workers and friends Hande avuş Arslan and Sümeyye Güleç Alasağ for their suggestions, helps and guidance.

I cannot even get close to adequately express my gratitude and thankfulness to my dear family members Atilla Güteryüz, Nurten Güteryüz, and Barış Güteryüz for their love, support, patience and being there for me throughout my whole life. I would also like to thank Şükrü Kılık, Amir Fadaie, Mehmet Ali Recai Önal, Hande Çiftpınar, Nesrin Ay and Oğuz Ay for being a special friends and wise advisors when I needed.

Also, I would like to thanks Doç. Dr. Fevzihan Başarır, Dr. Dilek Erbahar, Dr. Yıldız Uludağ, and Fahri Alageyik from TÜBİTAK; and Asst. Prof. Dr. Necmi Bıyıklı and Semih Yaşar from UNAM.

TABLE OF CONTENTS

ABSTRACT	V
ÖZ	vii
ACKNOWLEDGEMENTS	X
TABLE OF CONTENTS	XI
LIST OF TABLES	XIV
LIST OF FIGURES	XV
CHAPTERS	1
1. INTRODUCTION	1
1.1 Optical Waveguide Sensors	3
1.1.1 Planar OWG Sensor	4
1.1.2 Channel OWG Sensor	5
1.1.3 Fiber Optic OWG Sensor	6
1.1.3.1 Tapered	7
1.1.3.2 Cladding-off	8
1.1.3.3 End Modulated	9
1.1.3.4 D-Type	10
1.2 Light Guiding Fundamentals	11
1.2.1 Electromagnetic (EM) Wave Theory	11
1.2.2 Reflection and Refraction	13
1.2.3 Guided Modes	16
1.2.3.1 Optical Waveguide (OWG) Modes	17
1.2.3.2 Surface Plasmon Resonance (SPR)	19
1.3 Objective of the Theises	11
2. EXPERIMENTAL METHODS	23
2.1 Materials Used	24
2.2 Supporting Elements	25
2.2.1 Design	27

2.2.2	Mask Design and Fabrication.....	29
2.2.3	V-groove Fabrication	30
2.3	Development of D-type F/O Sensor Platforms	36
2.3.1	Placement of Fiber into V-Groove	36
2.3.2	Lapping and Polishing.....	37
2.3.3	Mounting FC/PC Connectors	39
2.3.4	Sensor Surface Modification	40
2.3.4.1	Thin Film Coating	40
2.3.4.2	RF Plasma Etching	41
3.	CHARACTERIZATION.....	43
3.1	Characterization of Supporting Elements	43
3.2	Analyzing Lapping and Polishing Protocol	48
3.3	Surface Modification.....	54
4.	TESTS AND MEASUREMENTS.....	57
4.1	Measurement System	57
4.2	Preparation of Solutions	60
4.2.1	Glycerin-Water Solutions.....	61
4.2.2	Biological Solutions	63
4.3	Sensitivity Measurements	63
4.4	Temperature Measurements	64
4.5	Wavelength Measurements	65
5.	RESULTS AND DISCUSSION.....	67
5.1	Typical Behavior of the D-type F/O sensor	67
5.2	Wavelength Measurements	71
5.3	Temperature Measurements	72
5.4	Results of Surface Modification.....	74
5.4.1	F/O sensors with SPR and OWG Modes	75
5.4.2	Roughened F/O Sensor.....	78
5.5	Biological Measurements	80

6. CONCLUSIONS 83

REFERENCES 85

LIST OF TABLES

TABLES

Table 1.1 Optical properties of materials at 633 nm wavelength [28].	4
Table 2.1 Mechanical property of fiber, silicon, SiC, and diamond [70].	38
Table 3.1 Width measurements of grooves for each step.	45
Table 3.2 Depth measurements after BOE and KOH.	46
Table 5.1 Sensitivities of the D-type F/O sensors for different polishing depths.	71
Table 5.2 Sensitivities for sensors with different polishing depths at different temperatures.	73
Table 5.3. Sensitivities for OWG and OWG+SPR type F/O sensors at different polishing deep and RI zones.	77
Table 5.4 Plasma etching applied -5 polishing depth SPR sensor sensitivities for different zones.	80

LIST OF FIGURES

FIGURES

Figure 1.1 Guidance of the light through a planar (slab) OWG [1].....	5
Figure 1.2 Different channel waveguide geometries [1].....	6
Figure 1.3 Illustration of fiber optic cable.	6
Figure 1.4 Demonstration of tapered fiber.....	8
Figure 1.5 Cladding-off fibers [46].....	9
Figure 1.6 Illustrations of end modulated fibers (a) the end-reflection mirror and (b) the angled fiber tip [46].....	9
Figure 1.7 D-type geometry of the F/O.....	10
Figure 1.8 The electromagnetic spectrum prepared by wavelength (meter) and frequency (Hertz). The pointed portion is the visible spectrum [64].	12
Figure 1.9 The EM wave representation in the space at the time t.	12
Figure 1.10 Electromagnetic wave behaviors at an interface between two different optical media. θ_i : Incident ray angle with respect to the surface normal, θ_r : Reflected (ray) angle with respect to the surface normal, θ_t : Transverse ray angle with respect to the surface normal, n_1 : Incident medium RI, n_2 : Refracting medium RI.	14
Figure 1.11 Demonstration of incident, reflected and transmitted plane waves with x and z components.....	15
Figure 1.12 Field distribution of TE guided modes.	17

Figure 1.14 Exponential decay of evanescent mode. 19

Figure 2.2 Optical lithography mask patterning schema..... 26

Figure 2.3 (a) Octahedron positioning of single crystal silicon planes [75], and (b) the designed V groove demonstration; w: width of V-groove, d: depth of V-groove, $\alpha_1=54.7^\circ$ (the exact angle between (111) and (100) planes), $\alpha_2=90.0^\circ - 54.7^\circ=35.3^\circ$ 28

Figure 2.4 (a) Cross sectional and (b) top view of embedded V grooves. 29

Figure 2.5 Patterned mask includes 16 silicon supporting element: (a) the designed mask for photolithography and (b) one of the silicon supporting element demonstration from the mask. 30

Figure 2.6 The production steps of V-grooves are (a) preparation of wafer, (b) photoresist application, (c) exposing UV-light, (d) removing photoresist layer, (e) SiO₂ layer etching with BOE, and (f) Si wafer etching with KOH. 31

Figure 2.7 (a) Positive photoresist long molecular chains breaks up with radiation so shorter chains can be removed with developing chemical, (b) Negative photoresist links become stronger with radiation so cross-linked network does not dissolve with developer [72]. 32

Figure 2.8 KOH etching experiment. 35

Figure 2.9 Produced supporting elements. 36

Figure 2.10 Placement of fiber into V-groove supporting element..... 37

Figure 2.11 FC/PC connectors are joined with F/O sensor platform. 40

Figure 2.12 Thin film coated D-type F/O sensor. 41

Figure 3.1 Microscope measurements of (a) mask, (b) lithography applied wafer, (c) BOE applied wafer, and (d) KOH etching applied wafer. 44

Figure 3.2 Profilometer measurements after buffered oxide etching (BOE). 45

Figure 3.3 Profilometer measurements during KOH etching for (a) 30 min., (b) 100 min., (c) 180 min., and (d) 300 min.	47
Figure 3.4 Front view of the polished fiber inside the V-groove. The dimensions are d_h = depth of V-groove for the edge of core and cladding region, α_2 = crystal orientation angle, h = polishing depth, R = fiber radius, and r = fiber core radius....	48
Figure 3.5 Side view of the polished fiber inside the V-groove.	49
Figure 3.6 Optical microscope measurements of (+5) polishing depth sensor after (a) 9 μm pad, (b) 3 μm diamond, and (d) 0.04 μm colloidal silica.	50
Figure 3.7 Optical microscope measurements of (-5) polishing depth sensor after (a) 9 μm pad, (b) 3 μm diamond, and (d) 0.04 μm colloidal silica.	51
Figure 3.8 Optical microscope measurements of (-10) polishing depth sensor after (a) 9 μm pad, (b) 3 μm diamond, and (d) 0.04 μm colloidal silica.	52
Figure 3.9 Optical microscope measurements of (-20) polishing depth sensor after (a) 9 μm pad, (b) 3 μm diamond, and (d) 0.04 μm colloidal silica.	53
Figure 3.10 SPM roughness image of the fiber's polished surface (1.40 nm).....	54
Figure 3.11 Scanning Probe Microscope (SPM) images of Au coated sensors of roughness (a) w/o, (b) 2 min., and (c) 4 min. plasma etching process.....	55
Figure 4.1 Opto-mechanical measurement system images (a), (b), (c), and (d) are taken from different views.	58
Figure 4.2 Measurement system schematic views.	59
Figure 4.3 Flow cell attached to the F/O sensor head (side view).	60
Figure 4.4 Antibody and antigen combination on the d-type F/O sensor.	61
Figure 4.5 The chemical structure of Glycerin [11].....	62
Figure 4.6 RI and glycerin-water concentrations relationship.	62

Figure 5.2 Effect of the polishing depth on the response of the D-type F/O sensor. .	69
Figure 5.3 Graph of average output power in zone I vs. the polishing depth.	69
Figure 5.4 The wavelength effect on the sensor’s response.....	72
Figure 5.5 The temperature effect on the sensor’s response.	73
Figure 5.6 (a) Simulation results for 20 nm Au & 2 nm Cr coated sensors, (b) resonance points for different gold-layer thicknesses (30-25-20-15-10-0 nm Au) – RI combinations, (c) Angular shift as functions of t_{gold} and n_{surr}	75
Figure 5.7 Normalized power results a function of RI for (a) -5 μm and (b) -20 μm deep polished with SPR+OWG sensors.	76
Figure 5.8 Results of a) 0 min. b) 2 min. c) 4 min. d) 0-2-4 min. plasma etching applied to the -5 μm deep polished sensor.	79
Figure 5.9 Detection of IgG molecules as a function of the output power.	81

CHAPTER 1

INTRODUCTION

The need for monitoring complex molecular interactions has inspired researchers to develop many types of evanescent wave based optical waveguide (OWG) sensing platforms. In general there are three major platforms: Planar, channel (strip, embedded strip, and buried strip) and fiber optic (F/O) [1, 2]. Recently, F/O platforms are in favor of the use over other sensor platforms since they are practical, economic to fabricate and easy to operate which make them ideal for clinical, pharmaceutical, industrial, and security applications [3-6].

F/O type sensors are mostly investigated on the basis of sensitivity, selectivity, readout times, long-term stability, cost and reusability. Among these type sensors, sensitivity enhancement of D-type F/O platforms depends on optical waveguide (OWG) and surface plasmon modes [7-9]. Sensitivity is the minimum amplitude of input signal required to generate output signal. Commonly, a F/O sensor consists of a light source, a detector, optical components, a sensing element and a F/O cable which guides light through physical variation medium to the detector [10].

When we consider the cross section of a F/O cable, there are three sections: core, cladding and protection layer [11]. The most critical part of a F/O sensor is the sensing section where the core part of the F/O is exposed partially to external molecular interactions. The sensing element (transducer) transfers these molecular changes to opto-electrical signals [12].

One of fundamental characteristics of the F/O sensor is total internal reflection (TIR). While the light (the electromagnetic EM wave) is reflecting internally in the core and propagating through the F/O cable, the EM wave field extends into the cladding or medium which surrounds the core. This EM field component is known as evanescent wave and its strength decays exponentially from the core-cladding boundary and some waveguide (OWG) modes can be triggered in this field [7]. Furthermore, if a thin metal layer such as gold is deposited on core cladding boundary, surface plasmon resonance (SPR) mode can be excited by introducing the thin metallic layer [13]. In fact, both waveguide and surface plasmon resonance (SPR) modes based sensors are significantly sensitive for the surrounding medium refractive index (RI) differences. That is, a small amount of RI changes in the medium in evanescent wave field may alter outputs of the sensor (intensity, polarization, phase, and wavelength of the light) [9]. The fiber cladding portion of the fiber is needed to be partially removed in order to expose the evanescent field to molecules [14-16]. Indeed, the smoothness of the exposed surface strongly influences the evanescent wave field distribution as well as the sensitivity of the sensor. These types of sensors are called either *side polished* or *D-type* F/O sensors.

The first demonstration of a F/O sensor was in 1900 by Villuendas and Palayo, who presented measurements of the sucrose concentration in an aqueous solution [17]. Within this study, the priority is given to develop F/O sensor platforms because they are suitable to commercialize as a product. In 1992, the theoretical and experimental research on evanescent wave based side-polished F/O sensor is reported by Tseng and Chen [14]. This study includes detailed fabrication steps of the sensor and measurement results matching with three different theoretical explanations. Surface plasmon mode F/O sensor production and theoretical study was firstly reported by Jorgenson and Lee, in 1993 [18]. The improvements on the sensor are provided to increase sensitivity for different RI ranges.

Despite many developments for the D-type F/O sensor, it is not commercialized for many years because its sensitivity is not enough to recognize small amount of molecular interactions. In fact, sensitivity of the D-type F/O sensor depends on interaction area, strength (RI of core and aqueous surrounding medium) and the

penetration depth of the evanescent wave field; and the operating wavelength. Some earlier works demonstrated that optimization of them dramatically affects sensitivity [19-24].

In this study, it is aimed to fabricate and characterize D-type multimode F/O sensors. The performance of sensors is enhanced by modifying some key parameters which are the polishing depth and the interaction area of F/O sensors. Besides, the architecture of sensors is designed to reveal both wave guide and SP modes between 1.33 and 1.47 RIU. The typical characteristics of sensors are determined, sensitivities are measured, wavelength effects are discussed, and behavior for different temperatures are studied. In addition, molecular interactions for IgG mouse and anti-mouse proteins is observed with SP mode D-type F/O sensor.

1.1 Optical Waveguide Sensors

Light transmission through a material/a medium is a very challenging issue for optical systems due to the behavior of the light such as diffraction, scattering, or interference during propagation process. To overcome the problem resulted during transmission of the light, the technology of guided-wave optics is presented. This technology has been a topic of great interest since Tyndall demonstrated the guidance of light in a rod by total internal reflection principle in 1870 [25].

An optical waveguide (OWG) is a media that allows light transmission for long distances without the use of complex optical components. That is, waveguides can confine the light inside a medium via a material with high RI embedded in a lower index substrate. The trapped light inside the OOWG can be propagated within multiple reflections at the boundaries of materials if the design is proper for guidance of wave from one end to another [12].

OWGs take part in technology for many years in order to manipulate the light according to intended purpose of the use [6, 26]. Biosensing with waveguides, on the other hand, is one of the special application fields [9]. In order to selectively detect biological molecules, the features of OWGs should be determined clearly during design process. After deciding frequency range of the transmitted light, the

geometries, refractive indices or material properties of waveguides should be suitable for detection [27]. For instance, one of the optical glasses BK7 with 10 mm thickness has transparency in visible range, semi-transparency in near infrared (IR) range, and opacity in far IR range, using BK7 glasses in visible range as a waveguide is more appropriate. For this study, mostly 633 nm wavelength (red) light is used during measurements and some of the material refractive indices, polarization and direction of light inside the materials are presented in Table 1.1 [28].

Table 1.1 Optical properties of materials at 633 nm wavelength [28].

Material	λ (μm)	n (RIU)	Polarization	Direction
Fused quartz	0.63	1.46	Parallel and Perpendicular	-
GaP	0.63	3.31	Parallel and Perpendicular	[010]
TiO ₂	0.63	2.58	Perpendicular	[001]
LiTaO ₃	0.63	2.18	Parallel	-
α -Al ₂ O ₃	0.63	1.76	Parallel	[11 $\bar{2}$ 0]
CdS	0.63	2.44	Parallel	-
H ₂ O	0.63	1.33	-	-

Besides the selection of materials for the waveguide, it is also essential to determine the geometry of waveguide platforms. There are mainly three different platforms which are planar, channel, and fiber optic [29-35]. All of them have advantages and disadvantages depending on application areas.

1.1.1 Planar OWG Sensor

A planar OWG comprises a slab material with high RI surrounded by media with a lower RI material [36]. The light is transferred by total internal reflection (TIR) inside this arrangement. The slab material is named as core and the outer material is called cladding. The schematic demonstration of the planar OWG is shown in Figure 1.1 [1]. In this figure “ d ” and “ n_I ” are the width and the RI of the slab respectively

and “ n_2 ” is the RI of the cladding. The confined light bounces between the cladding surfaces by making angles “ θ ” and propagates along the z-axis if the reflection angle is not larger than the critical angle. The wave propagation analysis for planar OWGs is fully investigated in the literature [37-39].

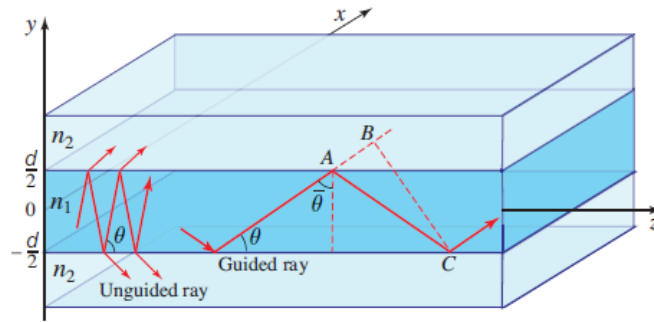


Figure 1.1 Guidance of the light through a planar (slab) OWG [1].

Planar OWGs have a great potential for sensing biological analytes such as hormones, toxins, viruses, bacteria or environmental monitoring and food safety [7, 28]. Their planar geometry is very promising to detect biological molecules if some of the restraints are eliminated such as complex construction issue or alignment problems [7]. In other words, to perform the waveguide in a sensor system, core and cladding materials should be deposited properly one by one. It is also noted that loss of the light coupling into the planar OWG should be as small as possible [29].

1.1.2 Channel OWG Sensor

It is possible to arrange the design of waveguide geometry as in Figure 1.2. It consists of a higher RI channel configured with a lower index substrate. These types of the channel OWGs are embedded strip, strip, rib or ridge, and strip loaded [1].

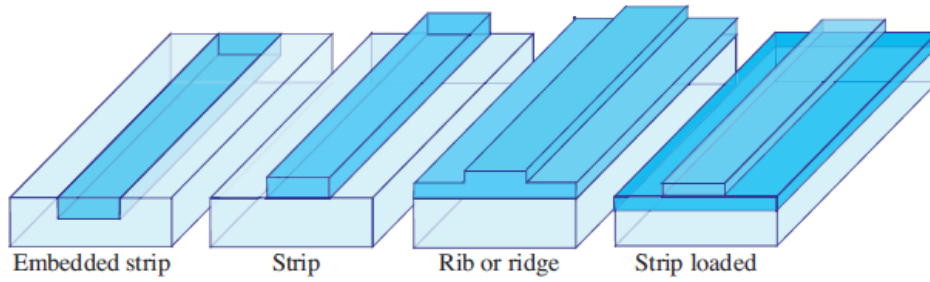


Figure 1.2 Different channel waveguide geometries [1].

Furthermore, they can be produced with different complex structures such as Mach-Zhender, directional coupler, and intersection [1, 27, and 31]. These multiple configurations offer to fabricate OWGs for different technological applications. Although geometry of the channel OWG is suitable for increasing sensitivity in various ways, their fabrication steps are too complicated and generate some problems [32, 40].

1.1.3 Fiber Optic OWG Sensor

A waveguide is named as F/O if high RI core media is enclosed by lower RI cladding material cylindrically. The structure can be protected with a polymer jacket as illustrated in Figure 1.3. Conventional F/O cables have two general types which are step index fibers and graded index fibers. While the RI of step index fibers are exact for core and cladding region, graded index fibers have a sloping increase and decrease of refractive indices [10].

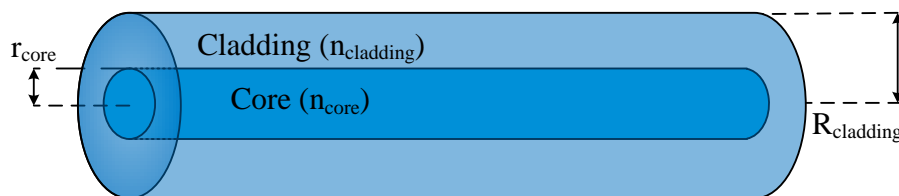


Figure 1.3 Illustration of fiber optic cable.

F/O offers a great potential in industry because this geometry possess the advantages of compactness, rugged packages, low cost, and high reliability [41]. These advantages lead to use fibers as sensors for different fields such as process control (temperature, pH, vibration, pressure, and fluid level), clinical applications, interactions of a variety of molecules (proteins, lipids, viral particles, and viruses), and security control [41-43].

The light can transform information in terms of intensity, phase, frequency, and polarization via a F/O cable [10]. There are many ways to convey the knowledge by utilizing the light. Thus, the way of impressing information should be decided before the F/O sensor is designed. Although using the phase, frequency, and polarization properties of the light can serve more sensitive devices, construction fiber sensors for intensity measurements is more convenient for industrial applications respectively [41].

The light transmission in fiber depends on the total internal reflection principle likewise the planar and channel waveguides. It is also noted that the light propagates through waveguides in different paths being named as modes. The guidance angle and group velocities for each mode are various but their transverse spatial distribution and polarization are similar [44]. The core diameter of the fiber determines mode numbers. If fiber core diameter is small enough to only support one mode, fibers are named as a single-mode one. Provided that larger diameter fibers permit more than one mode so they are classified as the multi-mode fibers[1].

Besides the light transformation classification, F/O sensors can be divided into four types according to the forming design. These are tapered, cladding-off, *end-modulated*, and *D-type* which are given in detail below.

1.1.3.1 Tapered

Tapered geometry means to thin any section of the F/O cable which results in to access the sensitive region [45]. This geometry also allows keeping cylindrical symmetry of fiber as illustrated Figure 1.4 [46].The tapered F/O profile can be linear, parabolic, and exponential [19].

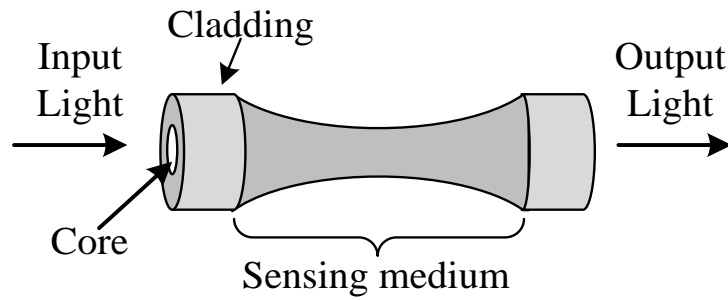


Figure 1.4 Demonstration of tapered fiber.

In the literature, a uniform taper geometry is mostly obtained by using traveling-burner system [46-48]. This system provides heat and stretching force in a controlled manner. Therefore, the precise dimensions of the taper geometry (diameter, length, and transition region properties) can be modified. In fact, changing the dimensions of geometry is utilized to increase the sensitivity [49].

1.1.3.2 Cladding-off

In order to get cladding-off geometry, it is necessary to remove some portion of the cladding from the middle region of the fiber by protecting the cylindrical symmetry as demonstrated in Figure 1.5 [46, 50-52]. The removed section of the fiber becomes sensitive to the surrounding medium. That is, the input light properties alter the media of exposed section changes.

The cladding of a fiber can be removed from around according to the fiber materials. While plastic-clad silica fibers' middle portion is burned away by using a hobby torch, a hydrofluoric (HF) acid solution and a buffered hydrofluoric (BHF) acid solution are used to remove the cladding part for silica fibers [16, 24].

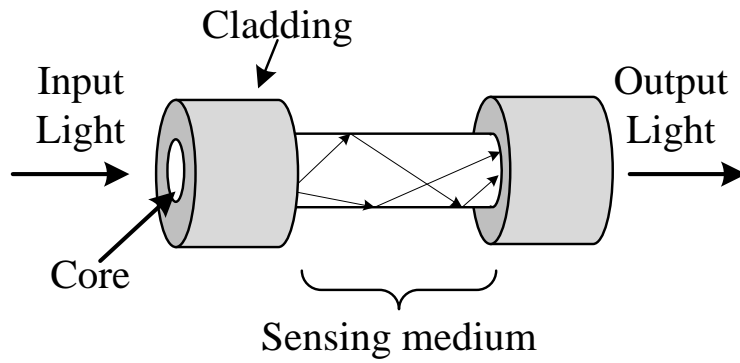


Figure 1.5 Cladding-off fibers[46].

1.1.3.3 End Modulated

The basic principle of end modulated F/O waveguides depends on phase matching at the end region [53]. The incident light guides through the end region and after interactions with the surrounding differences, it reflects back. Indeed, the modification of the tip geometry identifies the dynamic range and sensitivity of the waveguide [54]. Two configurations of end modulated fibers (end-reflection mirror and angled-fiber tip) are presented in Figure 1.6 [46]. These geometries can be formed by using blade, stripper, heat, polishing, or chemical etching [53-56].

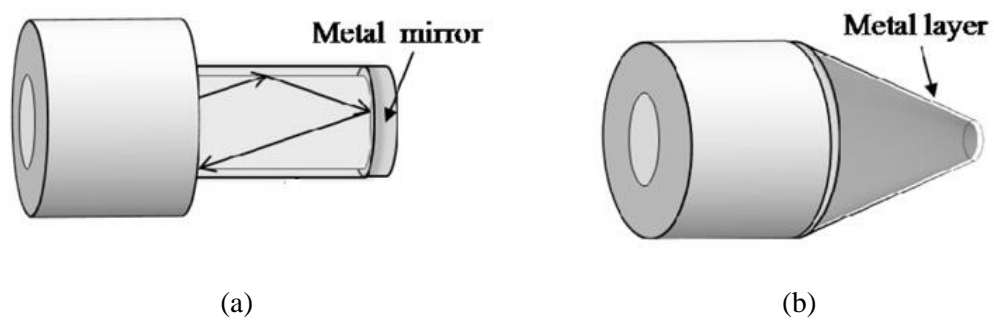


Figure 1.6 Illustrations of end modulated fibers (a) the end-reflection mirror and (b) the angled fiber tip [46].

1.1.3.4 D-Type

Among different geometries of F/O sensors D-type based platforms have attracted much attention because their sensitive regions are planar which results in multiplexing potential for molecular interaction sensing [3]. Further advantages of D-type geometry are long interaction length, easy to handle, flexible, and excellent light delivery [42, 57].

D-type platforms as depicted in Figure 1.7 can be fabricated with femtosecond laser engraving or polishing technique [14, 15]. High energy of a femtosecond laser beam can engrave the fiber without causing fractures. This process is very useful to perform D shapes on fibers. However, femtosecond micromachining system cannot be used to fabricate sensitive sensors because of the high surface roughness. On the other hand, polishing technique is very appropriate for fabricating D shapes in 1-2 μm level [58]. This technique may suffer from fiber deformations such as scratches, cracks, or broken regions if the polishing protocol is not proper for materials of F/O and surroundings. Thus, polishing process needs very careful attention during the application.

Besides the fabrication techniques, sensitivities of D-type F/O sensors can be tuned by changing the interaction length and the planar region depth [3, 59]. In fact, both parameters have effect on enlarging sensitive region. Furthermore, converting the modes and increasing the number of modes is possible for D-type F/O sensors [60]. Mode differences allow increasing sensitivity of sensors.

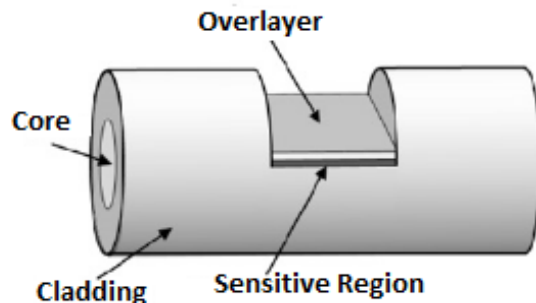


Figure 1.7 D-type geometry of the F/O.

1.2 Light Guiding Fundamentals

1.2.1 Electromagnetic (EM) Wave Theory

Electromagnetic (EM) wave is a kind of wave can propagate in a continuous medium at constant velocity with an exact shape by carrying radiant energy [61]. Electromagnetic waves possess both time and space varying electric and magnetic field components which oscillate perpendicular to each other along the propagation direction. Furthermore, its nature is explained and determined by some individual experiments that led to the invention of the set of fundamental laws which are Gauss' law for electric fields, Gauss' law for magnetic fields, Faraday's law, and Ampere's law [62]. They are modified and connected together by James Clerk Maxwell in 1864 as given in equations 1.1, 1.2, 1.3, and 1.4 [62].

$$\nabla \cdot E = \frac{1}{\epsilon_0} \rho \quad (\text{Gauss' Law for Electric Fields}) \quad (\text{eq. 1.1})$$

$$\nabla \cdot B = 0 \quad (\text{Gauss' Law for Magnetic Fields}) \quad (\text{eq. 1.2})$$

$$\nabla \times E = -\frac{\partial B}{\partial t} \quad (\text{Faraday's Law}) \quad (\text{eq. 1.3})$$

$$\nabla \times B = \mu_0 + \mu_0 \epsilon_0 \frac{\partial E}{\partial t} \quad (\text{Ampere's Law with Maxwell Correction}) \quad (\text{eq. 1.4})$$

The electromagnetic waves (EM) propagate in free space with same speed ($c = 3 \times 10^8$ m/s) is reached from Maxwell's equation [63]. However, the frequency of electromagnetic waves, which means wave oscillations per second, varies and all frequencies is known as the electromagnetic spectrum [61-63]. Different regions of the electromagnetic spectrum are denominated with special names such as gamma rays, X-rays, Ultraviolet (UV) Radiation, Visible Range, Infrareds (IR), Microwaves, and Radio Waves as demonstrated in Figure 1.8 [64].

It is essential to reach more quantitative understanding of how electromagnetic waves spread in a medium. Thus, the propagation of EM waves is presented in this section with the most familiar wave form which is a sinusoidal one. The wave function is introduced by eq. 1.5 at time $t = 0$ with Figure 1.9. The amplitude (A) of wave defines the displacement from the central maximum to the equilibrium region.

The cosine ranges between 0 and 2π is the phase of wave. The wave number (k) is in relation with the wavelength of the wave by the eq. 1.6 and “z” is the propagation direction of the wave. There is a uniform circular motion from a point light source so angular frequency (ω) is used to represent the number of radians swept per unit time (t).

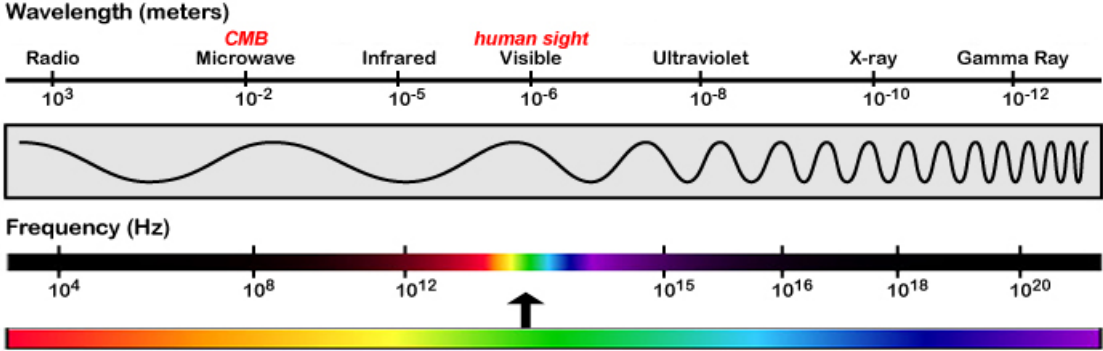


Figure 1.8 The electromagnetic spectrum prepared by wavelength (meter) and frequency (Hertz). The pointed portion is the visible spectrum [64].

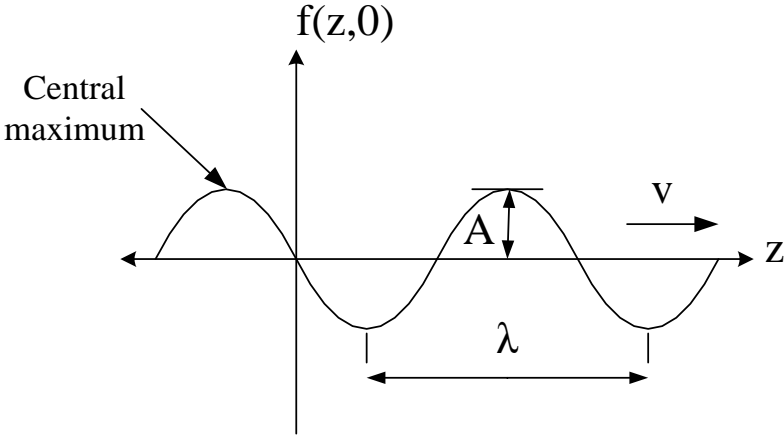


Figure 1.9 The EM wave representation in the space at the time t.

$$f(z, t) = A \cos(kz - wt) \quad (\text{eq. 1.5})$$

$$\lambda = \frac{2\pi}{k} \quad (\text{eq. 1.6})$$

In space, for Cartesian coordinates (x, y, and z) electromagnetic waves can propagate in three dimensions. Therefore, the eq. 1.7 can be written into eq. 1.5. The result is given in eq. 1.8.

$$r \equiv x\hat{x} + y\hat{y} + z\hat{z} \quad (\text{eq. 1.7})$$

$$f(r, t) = A \cos(k \cdot r - wt) \quad (\text{eq. 1.8})$$

It is also possible to use complex notation to the sinusoidal waveform as presented in eq. 1.10 by applying eq. 1.9 because the advantage of complex notation is that exponentials are much easier to manipulate.

1.2.2 Reflection and Refraction

When EM wave face an interface between two different medium, it can be reflected, or transmitted if the media are lossless as illustrated in Figure 1.10. The incident wave behavior is considered by using eq. 1.10 obtained in section 1.2.1.

Suppose that incident EM wave is in plane form which has normal in direction to the interface of planar boundary. Also, the interface is on (x, z) plane as in Figure 1.10. Incident (\tilde{f}_i), reflected (\tilde{f}_r), and transmitted (\tilde{f}_t) plane waves are presented with different wave numbers in 1.11, 1.12, and 1.13 equations. The waves oscillate at the same frequencies (w) for the system, on the other hand; since the wave velocities are different in two mediums, the wavelength of waves are also different.

$$\underline{\text{Incident Plane Wave}} \quad \Rightarrow \quad \tilde{f}_i = \tilde{A}_i e^{i(\tilde{k}_i \cdot \tilde{r} - wt)} \quad \tilde{k}_i = k_1 \hat{n}_i \quad (\text{eq. 1.11})$$

$$\underline{\text{Reflected Plane Wave}} \quad \Rightarrow \quad \tilde{f}_r = \tilde{A}_r e^{i(\tilde{k}_r \cdot \tilde{r} - wt)} \quad \tilde{k}_r = k_1 \hat{n}_r \quad (\text{eq. 1.12})$$

$$\underline{\text{Transmitted Plane Wave}} \quad \Rightarrow \quad \tilde{f}_t = \tilde{A}_t e^{i(\tilde{k}_t \cdot \tilde{r} - wt)} \quad \tilde{k}_t = k_2 \hat{n}_t \quad (\text{eq. 1.13})$$

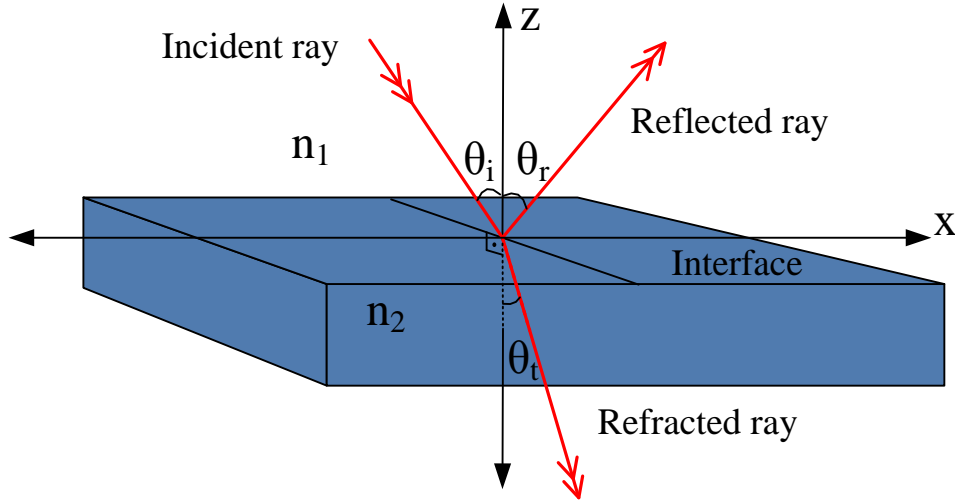


Figure 1.10 Electromagnetic wave behaviors at an interface between two different optical media. θ_i : Incident ray angle with respect to the surface normal, θ_r : Reflected (ray) angle with respect to the surface normal, θ_t : Transverse ray angle with respect to the surface normal, n_1 : Incident medium RI, n_2 : Refracting medium RI.

In order to solve plane wave equations 1.11, 1.12, and 1.13; boundary condition ($z = 0$ point) is needed to be used. At $z = 0$ point, addition of incident and reflected plane waves equal transmitted plane wave. Thus, equation 1.14 is obtained.

$$\tilde{A}_i e^{i(k_{ix}x + k_{iy}y - wt)} + \tilde{A}_r e^{i(k_{rx}x + k_{ry}y - wt)} = \tilde{A}_t e^{i(k_{tx}x + k_{ty}y - wt)} \quad (\text{eq. 1.14})$$

Note that, the vectors of incident (\tilde{A}_i) reflected (\tilde{A}_r) and transmitted (\tilde{A}_t) uniform plane waves are constant. Because the boundary conditions must cover all points on the (x, y) plane, these exponential factors have to be equal. Unless the exponential terms are cancelled, the equality for eq. 1.14 would be easily destroyed. To satisfy the equality, eq. 1.15 is presented.

$$k_{ix}x + k_{iy}y = k_{rx}x + k_{ry}y = k_{tx}x + k_{ty}y \quad (\text{eq. 1.15})$$

Initially, it is assumed that the plane wave has two components (x , and z) that propagate on the x - z plane, thus there is no y component as given in eq. 1.16.

$$k_{iy} = k_{ry} = k_{ty} = 0 \quad (\text{eq. 1.16})$$

From eq. 1.15 and 1.16 the equation 1.17 is obtained:

$$k_{ix} = k_{rx} = k_{tx} \quad (\text{eq. 1.17})$$

When the propagated wave is examined more explicitly by separating the wave number (k) terms for incident (eq. 1.18), reflected (eq. 1.19), and refracted (eq. 1.20) plane waves into (x, z) components of system in medium 1 and 2, total internal reflection (TIR) principle and Snell's law are obtained. It is noted that propagation constant for the z direction has been assumed zero so components in the z -direction is directly removed from the equations 1.18, 1.19, and 1.20. In Figure 11, the separations of components are demonstrated.

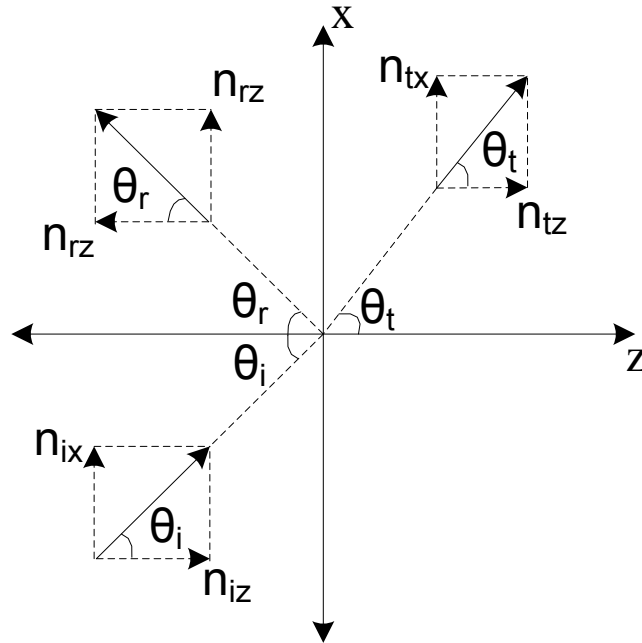


Figure 1.11 Demonstration of incident, reflected and transmitted plane waves with x and z components.

$$\text{Incident Plane Wave} \Rightarrow \tilde{k}_i = k_1 \hat{n}_i = k_1 \sin(\theta_i) \hat{n}_{ix} \quad (\text{eq. 1.18})$$

$$\text{Reflected Plane Wave} \Rightarrow \tilde{k}_r = k_1 \hat{n}_r = k_1 \sin(\theta_r) \hat{n}_{rx} \quad (\text{eq. 1.19})$$

$$\text{Transmitted Plane Wave} \Rightarrow \tilde{k}_t = k_2 \hat{n}_t = k_2 \sin(\theta_t) \hat{n}_{tx} \quad (\text{eq. 1.20})$$

When incident (k_{ix}) and reflected (k_{rx}) components are considered with equation 1.17, 1.18, and 1.19, it is possible to get law of reflection (eq. 1.21). That is, incident and reflected propagation constant equality ($k_{ix} = k_{rx}$) presents reflection law. This result shows that the angle of incidence is equal to the angle of reflection being independent from the medium parameters and frequency [61-64].

$$\theta_i = \theta_r \quad (\text{eq. 1.21})$$

When incident (k_{ix}) and transmitted (k_{it}) components are considered with equation 1.17, 1.19, and 1.20, Snell's law (refraction law) is obtained in equation 1.22 [61 - 64]. In fact, the RI of mediums (n_1 and n_2) is in relation with wave number terms (k_1 and k_2).

$$n_1 \sin(\theta_i) = n_2 \sin(\theta_r) \quad (\text{eq. 1.22})$$

As a result, two fundamental reflection and refraction laws are obtained in equation 1.21 and 1.22. It is remarkable that in lossless media EM wave can be reflected or transmitted with respect to RI of mediums and incident angle.

1.2.3 Guided Modes

Waves can propagate by following an arbitrary reflecting pathway if waveguide cross-section is too large than the light wavelength according to the solutions of Maxwell equations. However, as the thickness of waveguides decrease to the order of the wavelength, the light rays propagate in the form of wave packets. In reality, light beams are a mixture of different frequencies of waves so certain pathways appear during propagation of the light. The outcomes of this situation can be observed as a movement of continuous electric and magnetic fields along the waveguide. This phenomenon is called as guided modes [28, 44, and 59].

Each waveguide platforms (planar, channel, fiber optic) has special mode derivations. Maxwell equations, boundary conditions, and a number of approximations are combined to solve the presented modes such as transverse electric ($TE_m, m = 0, 1, 2 \dots$), transverse magnetic ($TM_k, k = 1, 2 \dots$), waveguide, and surface plasmon modes [1]. The supported mode numbers by a waveguide depends

on core radius (r_{core}), core RI (n_{core}), cladding RI ($n_{cladding}$), and wavelength of the guided light (λ). For multimode fibers, the number of modes (M) can be calculated approximately by using the equation 1.23.

$$M = \frac{4}{\pi} \left[2 \frac{r_{core}}{\lambda} \sqrt{n_{core}^2 - n_{cladding}^2} \right] \quad (\text{eq. 1.23})$$

TE guided modes field distribution for the few order modes are demonstrated in Figure 1.12. They are sinusoidal standing waves and their frequencies increase as the mode numbers increase. While lower order modes ($m = 0$) is more confined, higher order modes ($m = 1, 2, 3\dots$) have dispersing intensity from the center of the waveguide [7, 68].

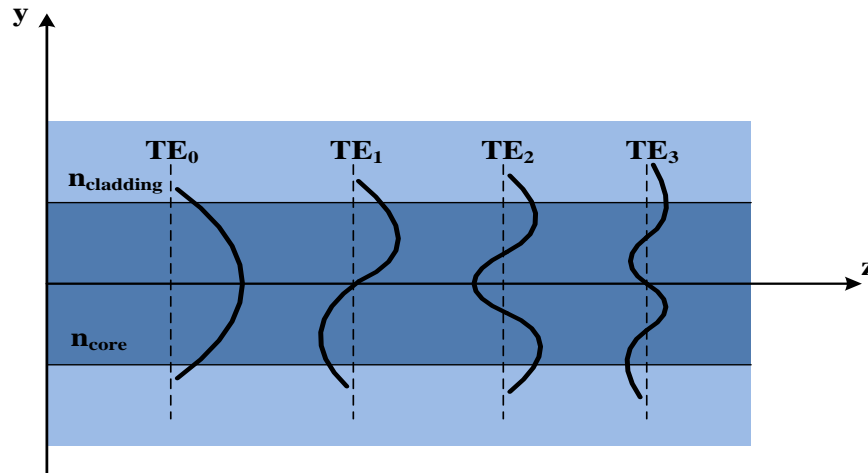


Figure 1.12 Field distribution of TE guided modes.

1.2.3.1 Optical Waveguide (OWG) Modes

In order to understand evanescent wave region occurrence in fiber, the light propagation phenomenon of reflection principle and Snell's law should be considered together. The light reflectance and transmittance depends on refractive indices of mediums and the incident angle as mentioned in 1.2.2 section. When the light beam in a medium with RI n_1 strikes a boundary of a medium with RI n_2 , where $n_1 > n_2$ and incidence angle is greater than critical angle ($\theta_c = \sin^{-1}(n_2 / n_1)$) as in

Figure 1.13; total internal reflection (TIR) of light occurs as a consequence of Snell's law [61]. Remarkably, if the light reflects back totally in an intense medium, a significant portion of electromagnetic field penetrates into the surrounding medium or cladding region for the fiber. This penetration field is known as evanescent field [10].

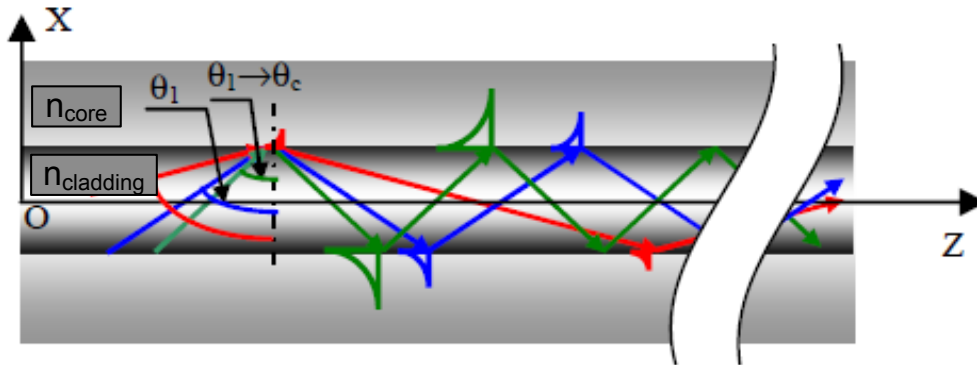


Figure 1.13 Evanescent waves occurrence between the core and cladding interface [69].

The power of evanescent field extension depends on the incident light angle. As the angle of incidence is closer the critical angle, penetrated electromagnetic field becomes more effective in the surrounding medium. Furthermore, evanescent wave amplitude exponentially decays ($1/e = 0.37$) with distance from the core interface as demonstrated in Figure 1.14. Penetration depth (d_p) can be described mathematically with a function of the light wavelength (λ), the incidence angle (θ), the RI of the core (n_{core}) and the cladding ($n_{cladding}$) given by eq.1.24 [7].

$$d_p = \frac{\lambda}{4\pi[n_{core}^2 \sin^2 \theta - n_{cladding}^2]^{1/2}} \quad (\text{eq. 1.24})$$

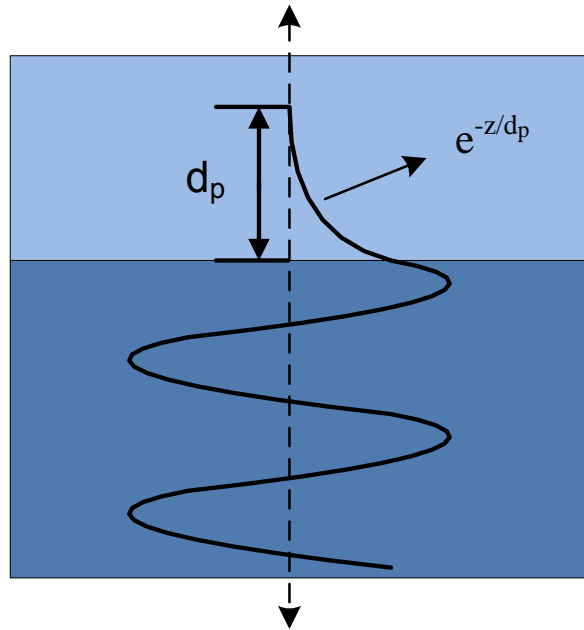


Figure 1.14 Exponential decay of evanescent mode.

Power fraction of evanescent wave inside the surrounding medium changes between a few tens to a few hundred nanometers ranges depending on RIs[2]. If this extended power encounters some variations, output light properties such as wavelength, phase, or intensity can change. Therefore, the penetration depth parameter should be considered in detail during fabrication of evanescent wave sensors because it is the one of parameters that sensors' sensitivity closely depends on [7].

1.2.3.2 Surface Plasmon Resonance (SPR)

Plasmons or plasma oscillations are related mostly with the free electrons inside a conductor such as gold and silver. If free electrons are locally decreased by an outside force, free electrons start to move to decrease the potential energy for this local region. This causes attraction of free electrons and positive ions called as driving force. However, negative ions are accumulate too much to obtain charge neutrality so Coulomb repulsion as restoring force appears between free electrons. Because attractive driving force and repulsive restoring forces are in opposite directions, oscillations occur between free electrons. These oscillations called plasma

oscillations and the quantum of these oscillations are named as plasmons [13]. Furthermore, plasma oscillations are supported at metal and dielectric interfaces and appear as energy loss. The addition of these oscillations is referred as surface plasmon resonance or surface plasmon polaritons [19].

Longitudinal (TM or p polarized) electromagnetic wave excites surface plasmons which decays exponentially. The behavior of the incident light and entire electromagnetic field distribution across the surface of a metal can be calculated by using Maxwell equations and is well established in the literature [28, 65]. Surface plasmon propagation constant (K_{SP}) is given by the equation 1.25 where metal dielectric constant (ϵ_m), substrate dielectric constant (ϵ_s), incident light frequency (w), and velocity of light (c) are in relation. Also, light propagation constant at frequency (w) for the dielectric medium is given in equation 1.26.

$$K_{SP} = \frac{w}{c} \left(\frac{\epsilon_m \epsilon_s}{\epsilon_m + \epsilon_s} \right)^{1/2} \quad (\text{eq. 1.25})$$

$$K_S = \frac{w}{c} \sqrt{\epsilon_s} \quad (\text{eq. 1.26})$$

While metal dielectric constant (ϵ_m) is smaller than zero, the substrate dielectric constant (ϵ_s) is greater than zero for a given frequency. Therefore, it is obvious that the propagation constant of the metal is higher than the substrate ($K_{SP} < K_S$). In order to excite surface plasmons at interface propagation constants are needed to be equal at least. That is, surface plasmon mode cannot be excited with a direct light so an extra energy or momentum should be applied the light to be coupled. Thus, the generation of evanescent field, which occurs during the TIR of light, is required to excite surface plasmons [66, 67]. mouse proteins is observed with SP mode D-type F/O sensor.

1.3 Objective of the Thesis

As mentioned in the introduction part, the objective of the thesis is to develop D-type multimode F/O sensors to detect variations in aqueous environment for a wide range RIs between 1.33 and 1.47. The geometrical modification technique is used to

improve the sensors response. The general investigated objective of the thesis can be presented as follows:

- D-type fiber optic (F/O) sensors with 25 mm-long interaction lengths have been developed.
- The effects of geometrical design parameters and certain processing variations including polishing depth, additional gold thin film coating, and surface roughness on detection/sensing performance of biomolecules are reported.
- The performance analyses were performed in liquid environments exhibiting refractive indices (RI) values 1.33-1.47.
- Specifically, the sensitivity of sensors is enhanced with partial gold film coating because it is excited SPR mode in addition to OWG mode.
- RF plasma etching is used as a novel method to increase roughness and sensitivity of sensors.
- The location of the SPR and OWG modes and sensor response is tuned by controlling the geometrical parameters to monitor IgG proteins in liquid environment.

CHAPTER 2

EXPERIMENTAL METHODS

The experimental procedure consists of material selection, designing, fabrication, and development of the F/O sensors with respect to optimized parameters. Each process is explained in detail. First steps of fabrication process are determined and suitable materials are selected. The faced problems during production procedures are dealt with changing the used materials or method of fabrication steps. Furthermore, materials are shaped by following some designing strategies. Appropriate parameters for designing are determined according to some mathematical calculations and experimental results. Using these parameters the components of the sensor system are shaped, fabricated and joined together one by one. In Figure 2.1 a flow chart is drawn to generalize the experimental procedure.

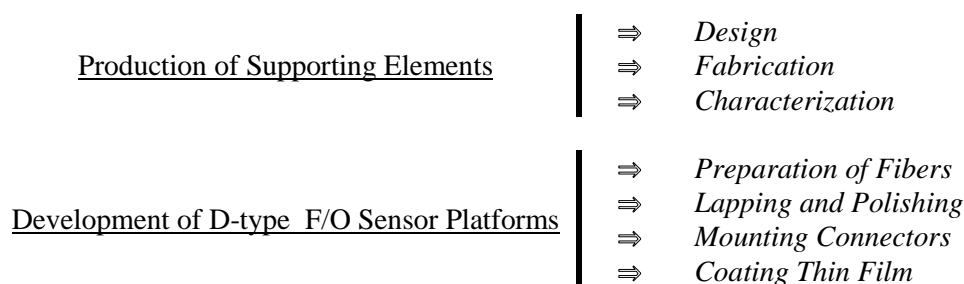


Figure 2.1 Flow chart of the experimental procedure.

2.1 Materials Used

Throughout the thesis, different chemicals and optical materials are used for producing supporting elements and D-type F/O sensor platforms. The purchased materials for this study are described with their sources and properties in this section.

First of all, supporting elements are fabricated from silicon wafers with photolithography and chemical etching processes. 4-inch Si wafers having ~5000 Å oxide layer are purchased from Helitek. Chromium coated glass, Hexamethyldisilazane (HMDS), photoresist AZ5214, and developer-AZ400k for the photolithography process and for the chemical etching processes buffered oxide etch (BOE), and potassium hydroxide (KOH) are provided by UNAM, Bilkent University.

The purchased materials for development of the D-type F/O sensor platform can be divided into four classes which are optical materials, lapping and polishing materials, mounting connectors, and thin film coating materials. As optical materials, 100 meter, step index, multimode AFS50/125Y model fiber with the 0.22 numerical aperture, 50 µm core diameter, and 125 µm cladding diameter (ThorLabs) and epoxy EPO-tek 301-1 (Epoxy Technology) are used. Besides these materials, in order to mount F/O connectors 30126G2 model 20 items of FC/PC multimode F/O connectors and CK03 model fiber optic termination and repair kits which include fiber stripper, crimp tool, polishing films with 0.3 µm, 1 µm, 3 µm, 5 µm grits, and epoxy are bought from Thorlabs. Moreover, for the lapping and polishing procedure SiC-2500 grit polishing pad, polyurethane pad, 3 micron diamond, water-oil based lubricant liquid and 0.04 µm colloidal silica is purchased from Struers. Furthermore, during the thin film coating procedure gold and chromium are used. The gold is supplied from İstanbul Altın Rafinerisi with %99.99 purity and Chromium (Cr) is purchased from Kurt J. Lesker Company with %99.99 purity.

To clean the equipment; acetone, isopropyl alcohol, and ethanol are used. They are purchased from Merck Company with ~%95 purity. The used water is obtained from Direct Q3-UV Millipore system at 18.2 MΩ cm resistivity and 25 °C temperature.

2.2 Supporting Elements

Through experimental procedure fragile glass fibers are locally polished, lapped, and coated with films. These applications cannot be entailed to fibers unless they are supported with appropriate elements. Supporting elements are necessary for better handling during fabrication of D-shape F/O sensors.

The key point of supporting elements is that their material properties (i.e. thermal expansion, hardness, etc.) should resemble silica fibers. Both of them are needed to overcome harsh fabrication steps such as lapping and polishing. Supporting elements protect fibers from surface cracks/defects during mechanical polishing and damage eliminating. In fact, surface conditions such as roughness, scratches, cracks; and the nature of subsurface damages are very effective on sensitivities of the produced sensor. Material removing mechanism can provide same polish rate only if the materials of supporting elements and fibers coincide each other. In literature mostly quartz or silica blocks are used [14, 21]. Silica blocks are selected to support fibers for this study because they have advantageous properties. The followings are significant features of single crystal silicon wafers [70]:

- i. Silicon wafers can be produced in controllable processes with standard purity and perfection.
- ii. Silicon fabrication relies on deposition of very thin films which pursuit them to use for miniaturized devices.
- iii. Silicon wafers can be shaped and patterned by applying lithographic techniques so highly precious geometries production becomes possible.
- iv. In practical point of view, inexpensively obtained silicon wafers can be etched in batch processing.

Supporting elements can be produced from commercially available Si wafers which present high purity and perfect crystalline orientation. It is possible to engrave Si wafers with precision geometries by using lithography and chemical etching processes [70]. While lithography process constitutes designing and forming the intended geometries, etching procedure chemically shapes the structured patterns on Si wafer.

Images are formed on Si wafer with lithography process. This approach provides selectively removal of materials, building up thin films, or changing some portion of the wafer characteristics. There are variety of lithographic technologies being used in wafer processing such as photolithography, electron lithography, x-ray lithography and ion lithography [71]. Photolithography technique, also called as optical lithography, is used to replicate patterns on Si wafer for this study.

Optical lithography process includes many steps which are mask fabrication, cleaning wafer, resist coating, post-application bake, UV light exposure, post-exposure bake, selectively removal of resist coating, and resist hardening [72]. The used mask for photolithography involves a patterned transparent substrate. In fact, photo-mask protects the patterned zones when UV light is exposed on the Si wafer. Preparation of wafer includes cleaning, resist coating and resist hardening steps. These steps can be followed with UV light application as demonstrated in Figure 2.2. Light source generates light beam and some portion of it passes through the openings of mask. The resist properties chemically change under UV light exposure. Than the light-sensitive resist, is also known photoresist, can be removed with developing solution according to the type of resist: positive or negative. While positive resist easily dissolve in developer solution, negative resist becomes less soluble after light exposure. Therefore, mask replication process on silicon wafer occurs with photolithography procedure [71-73].

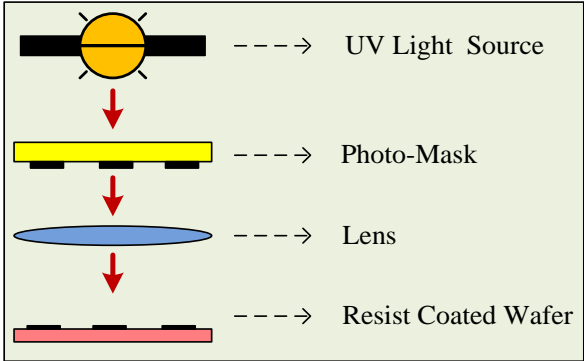


Figure 2.2 Optical lithography mask patterning schema.

After lithography process application, patterned silicon wafer is chemically etched to form shapes. Indeed, etching has been used widely for production of micromachining devices such as sensors, optical waveguides, transistors, and emission devices [74]. There are various isotropic and anisotropic chemical etchants for silicon as mentioned in literature and they have important effects on micromachining devices [70]. Between etchant systems KOH anisotropic etching has a particular interest because its highly selective property allow fabrication of unique geometries if patterns are masked by some materials, e.g., SiO₂, Si₃Ni₃, and Cr. Also, its selectivity depends on crystal orientation of Si surfaces. For instance, the (100) plane etches faster than the (111) plane which is in relation with the activation energies of planes. While (100) Si surface dissolve with one OH⁻ per atom, (111) plane needs two OH⁻ per atom [75]. Silicon etching rate (R) relies on temperature (T), KOH-water concentration, and activation energy (E) of plane. Their best relation is obtained by Seidel and it is given in equation 2.1 where “ K ” is kinetic rate constant, and k is Boltzmann constant [76].

$$R = [H_2O]^4 [KOH]^{1/4} K \exp(-E/kT) \quad (\text{eq. 2.1})$$

In the experimental section of the thesis, supporting element is fabricated from (100) oriented Si wafer by using lithography and KOH chemical etching procedure. These processes provide to groove Si wafer in V shape. The details of V type silicon supporting element’s design, fabrication, and characterization steps are described in section 2.2.1, 2.2.2, 2.2.3., and 2.2.4.

2.2.1 Design

The main point of V-type supporting elements fabrication is to protect and hold delicate and fragile fibers. This aim clearly promotes designing step importance. Supporting element platforms are designed with 30 mm long, 10 mm wide, and 0.5 mm height dimensions.

In order to fix fibers properly inside the supporting element grooves, shape of canals should be considered carefully. V shape is the presented best supporter form in literature [14]. Anisotropic etching is applied to place 125 μm multimode fiber optics

into V shape grooves with respect to the crystal octahedron positions of (100) and (111) planes as seen in Figure 2.3. Therefore, fibers would be settled into canals without any shift. Indeed, the Si wafer crystal orientation decides the shape and scale of grooves during chemical etching process. The reason underlies different etching rates of (100) and (111) surface arrangements. The denser (111) plane etch rate is slower than (100) plane etch rate which causes an anisotropic etching with an exact angle, 54.7° between planes [75].

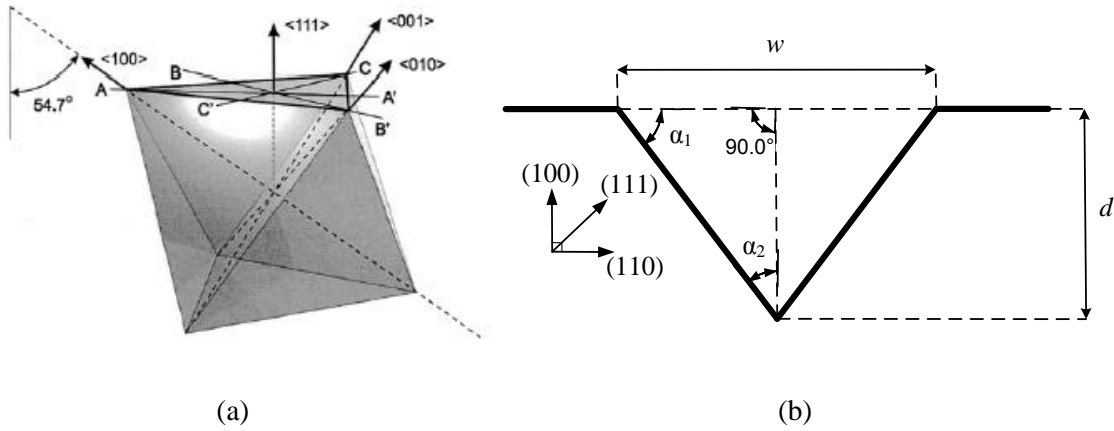


Figure 2.3 (a) Octahedron positioning of single crystal silicon planes [75], and (b) the designed V groove demonstration; w : width of V-groove, d : depth of V-groove, $\alpha_1= 54.7^\circ$ (the exact angle between (111) and (100) planes), $\alpha_2=90.0^\circ-54.7^\circ=35.3^\circ$.

Additionally, there is a relationship between the depth (d) and width (w) of the V-groove due to the exact angle. This relation gives an advantage to calculate depth of canal with measuring width of the V-groove being given in equation 2.2.

$$d = \frac{w/2}{\tan(\alpha_2)} \quad (\text{eq. 2.2})$$

In order to be more controllable on polishing length during the operation of fibers and to get smooth transformation of the light, fibers are placed into grooves with gradual curving. This special placement technique also provides to eliminate light losses. Therefore, a novel design is developed for V-grooves. From the center to the edge, the widths of grooves are gradually increased about 0.014° as shown in

Figure 2.4 (b). Particularly, curving fiber gradually with a special design decreases the fiber damages during polishing process. The dimensions of the supporting element are illustrated in Figure 2.4 (a) and (b) from the cross sectional and top views.

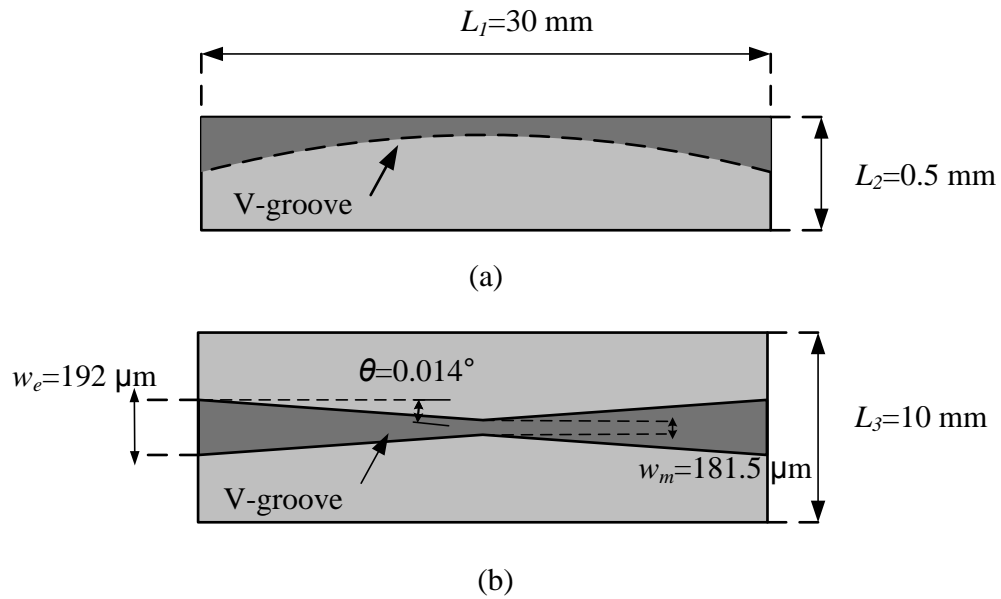


Figure 2.4 (a) Cross sectional and (b) top view of embedded V grooves.

2.2.2 Mask Design and Fabrication

The first requirement of photolithography process is fabrication of a mask. The mask is designed by using a 4-inch Si wafer to produce as much as possible supporting elements from the same wafer. The design of mask is allowed us to fabricate 16 supporting elements with the desired dimensions as illustrated in Figure 2.5. In order to produce the mask, purchased 100 nm chrome coated quartz is patterned using mask writer (Heidelberg Instruments, DWL-66) with a 4 mm writing head. This head can pattern quartz at least 1 μm sizes so the supporting elements are produced nearly exact dimensions.

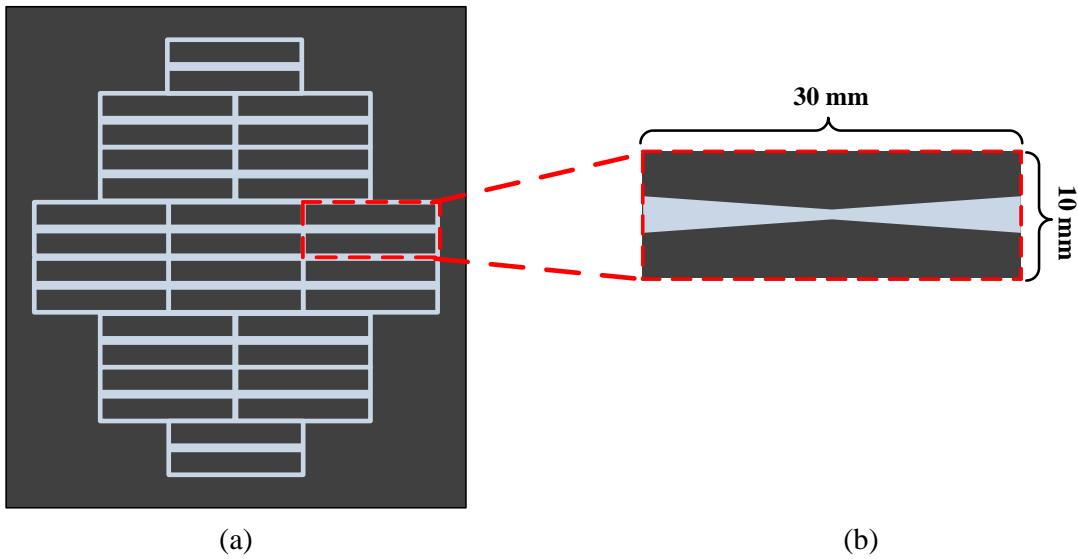


Figure 2.5 Patterned mask includes 16 silicon supporting element: (a) the designed mask for photolithography and (b) one of the silicon supporting element demonstration from the mask.

2.2.3 V-groove Fabrication

Fabrication of V-grooves includes mainly two processes which are photolithography and chemical etching. Both of them have many steps as depicted in Figure 2.6. Firstly, photolithography is used to transfer patterns from the mask to the substrate (Si wafer) by using an UV-light. Its steps are preparation of wafer, photoresist application, exposing UV-light, removing the photoresist layer. Then, chemical etching process is maintained to etch patterned regions. Chemical etching procedure consist two steps which are buffered oxide etching (BOE) and potassium hydroxide etching (KOH-etching).

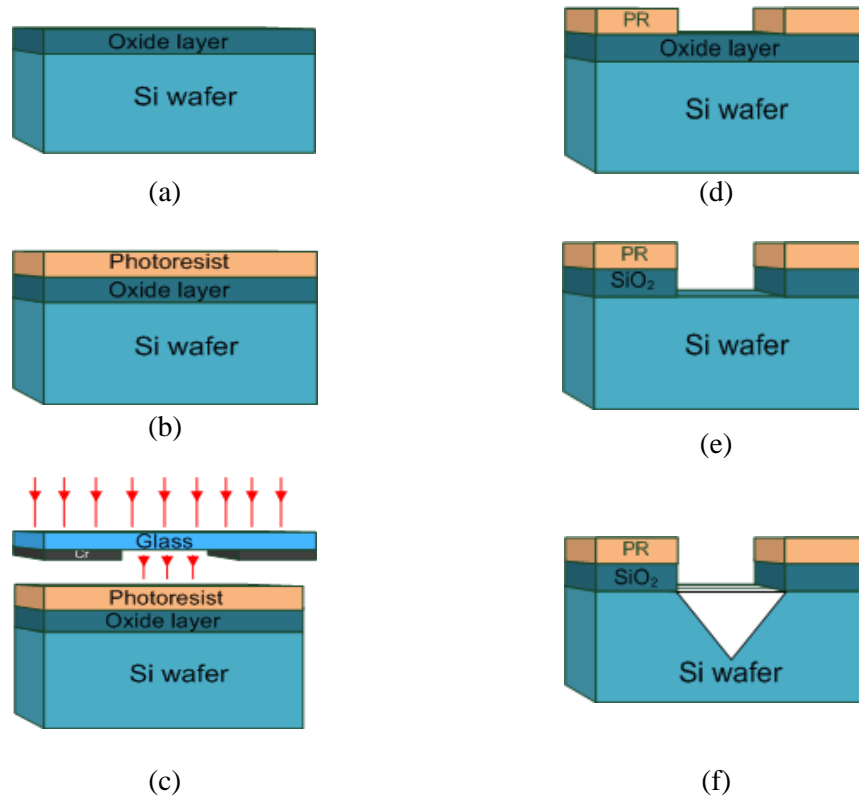


Figure 2.6 The production steps of V-grooves are (a) preparation of wafer, (b) photoresist application, (c) exposing UV-light, (d) removing photoresist layer, (e) SiO₂ layer etching with BOE, and (f) Si wafer etching with KOH.

The steps of photolithography and chemical etching procedures:

- (a) Preparation of Silicon Wafer: Silica coated Si wafer with (100) crystal orientation is cleaned carefully with chemicals and water to wipe away dirties. In fact, contaminants and particles removing from the surface reduce defects and improve photoresist adhesion. Wafer is ultrasonically rinsed with acetone, isopropanol, and DI water for 10 minutes. Then, it is dried in furnace at 110 °C for 5 minutes.
- (b) Photoresist Application: Photoresist is a kind of polymer that undergoes chemical reaction if light is induced on it. This chemical reaction changes according to the photoresist type being positive or negative resist. For positive photoresist, inducing light scissions polymer chains from a larger molecule chains to smaller ones as depicted in Figure 2.7 (a). On the other

hand, molecular chains of negative photoresist link with higher order magnitudes after exposure as in Figure 2.7 (b).

The resist processing includes Hexamethyldisilazane (HMDS) coating, resist coating and post application baking. The cleaned Si-wafer is coated with positive photoresist-AZ5214 1.4 μm but to increase adhesion HMDS is applied on surface at first. HMDS is a colorless liquid with the molecular formula $[(\text{CH}_3)_3\text{Si}]_2\text{NH}$ [77]. After HMDS application photoresist is coated with spin coating method. Spin coating system (Laurell, WS650SZ-6NPP-lite) is utilized at 4000 RPM for 60 seconds. This system spreads liquids by centrifugal force to coat evenly the wafer sited on vacuum chuck. Furthermore, film drying rate affects quality of the film on the surface such as uniformities appear with slow rate. Thus, furnace is used at 110 $^\circ\text{C}$ for 5 minutes to dry film, and then wafer is cooled down.

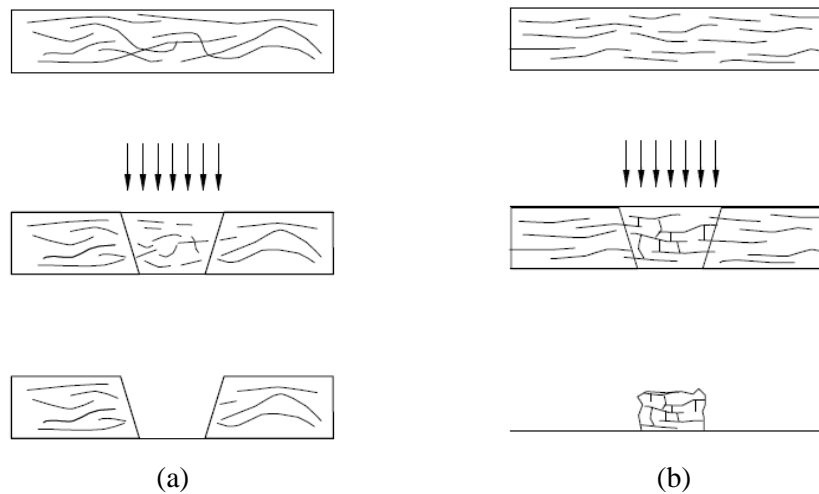


Figure 2.7 (a) Positive photoresist long molecular chains breaks up with radiation so shorter chains can be removed with developing chemical, (b) Negative photoresist links become stronger with radiation so cross-linked network does not dissolve with developer [72].

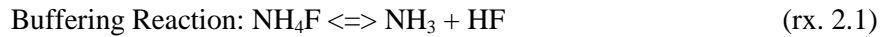
(c) Exposing UV-light: An exposure system provides replication of mask images on photoresist coating. This system includes a light source, condenser, mask, wafer and wafer stage aligner. The light source generates

light beam in the UV spectrum (200 nm - 460 nm ranges) and the condenser delivers light to mask and photoresist uniformly. The stage aligner, on the other hand, provides to position wafer in a controlled way. The key factor of replication quality is mostly depends on alignment of exposure system components.

In this study, Mask Aligner (EVG, EVG620) is used as an exposure system. A recipe is prepared by following: the sizes of mask holder (5 inch) and wafer (4 inch); thickness of mask (2.3 mm), wafer (0.5 mm), and photoresist film (1.4 μm); and process type (top side), process mode (transparent), exposure mode (continuous), contact mode (vacuum contact). Previously fabricated mask and photoresist coated wafer are loaded and aligned inside the exposure system. Then, wafer is exposed by utilizing the entered recipe.

- (d) Removing photoresist layer: In order to remove UV-light exposed photoresist, AZ400k-developer is used. The removing process is manipulated by the resist dissolution rate, which is in relation with development concentration, exposure, resist properties, and pre-baking step. The photoresist is locally dissolved with 1:4 ranges mixed developer and DI water solution in 60 seconds by using immersion method. After the application of developer, wafer is cleaned with extra water and dried. At the end of the process, wafer is hard-baked in furnace at 120 °C, 60 seconds to strengthen bonds of photoresist film. Baking photoresist prepares the wafer for BOE and KOH chemical etchings.
- (e) Buffered Oxide Etching (BOE): BOE is a wet etchant consists of Ammonium Fluoride (%40 NH_4F - DI water) and Hydrofluoric (HF) acid in a 6:1 ratio. It is used to etch 5000 Å thickness silica film selectively. The BOE process governs by two different chemical reactions which are buffering reaction (rx-1) and etching reaction (rx-2). While buffering reaction controls HF concentration to stabilize pH of solution, SiO_2 is removed with etching reaction.

BOE solution is prepared inside a Teflon container and the wafer is immersed into the buffered HF chemical. The wafer is hold 4 minutes in container about 4 minutes. The silica film is etched with 120 nm/min rate at 22°C. After the etching is completed, wafer is rinsed with DI water carefully and dried by using nitrogen. Etched silica film is controlled by using microscope and profilometer. If the silica film is not etched completely, the process is repeated. Then, photoresist film is removed with acetone.



- (f) KOH etching: In order to form V grooves in (100) oriented Si wafer KOH etching method is used after the patterned oxide layer is removed. KOH etching rate depends on temperature, KOH solution concentration, and Si crystallographic plane directions as mentioned in literature [75-77, 78]. For this study, Si wafer is etched with 25 micron/hour rate. The kinetics of etching rate is discussed in terms of an Arrhenius equation by estimation of the activation energy according to Seidel et al. [76]. Si etch rate (R) in KOH is modeled as

$$R = [\text{H}_2\text{O}]^4 [\text{KOH}]^{1/4} \exp(-E/kT) \quad (\text{eq. 2.3})$$

where “E” is the activation energy in eV, “k” is the kinetic rate constant, and “T” (Kelvin) is the temperature.

KOH solution is prepared inside a wide glass beaker by using 300 gram potassium hydroxide pellets (by weight) and 700 gram DI water. The KOH pellets and water are mixed till potassium hydroxide is dissolved. The beaker is located on a hot plate at 60 °C with magnetic stirrer at ~250 RPM and waited for 30 minutes to stable the solution conditions. Then, wafer is placed into solution with hallow Teflon vessel and evaporation is prevented by closing beaker carefully with aluminum foil (Figure 2.8). During the experiment, temperature of solution is observed continually. V shapes are formed as seen Figure 2.6(f) in 5.44 hours. After KOH etching processes is

completed, the Si wafer is removed from solution and rinsed with enough DI water until all deposits are removed.

The prepared silicon wafer is cut by using dicing machine (Disco, DAD3220). 16 supporting elements are obtained from 4 inch Si-wafer with 30 mm long and 10 mm wide dimensions. Then, each supporting element is glued onto 37.5 mm and 75 mm long two microscope slides (Fisher Scientific Company L.L.C., 12-544-1) as in Figure 2.9. These microscope slides make easy the placement of fibers inside the V-grooves.

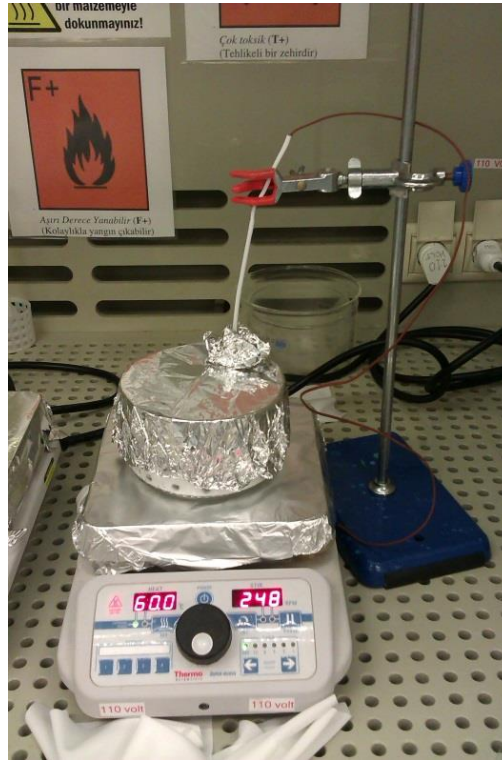


Figure 2.8 KOH etching experiment.

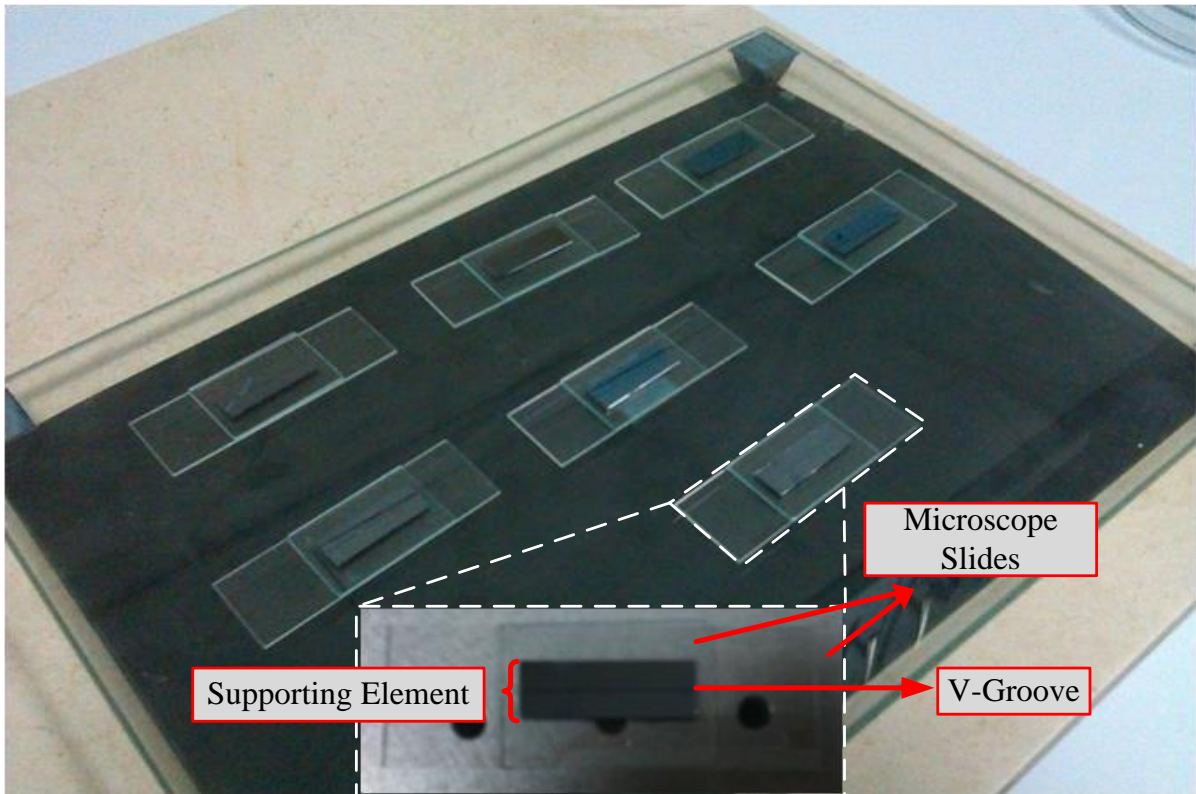


Figure 2.9 Produced supporting elements.

2.3 Development of D-type F/O Sensor Platforms

In this section, fibers' placement into supporting elements; lapping and polishing procedure; mounting FC/PC connectors to fiber; and thin film coating experiments are represented in detail.

2.3.1 Placement of Fiber into V-Groove

The purchased F/O cable from Thorlabs (AFS50/125Y) has three sections which are core, cladding and coating material (jacket). While the core and cladding sections are made from silica, the material of jacket is produced from an acrylate polymer which melts about 160 °C [79]. Before mounting fibers into V-grooves, 30.3 mm from the section of a 1 m long fiber jacket is stripped with heat. The stripped region is wiped

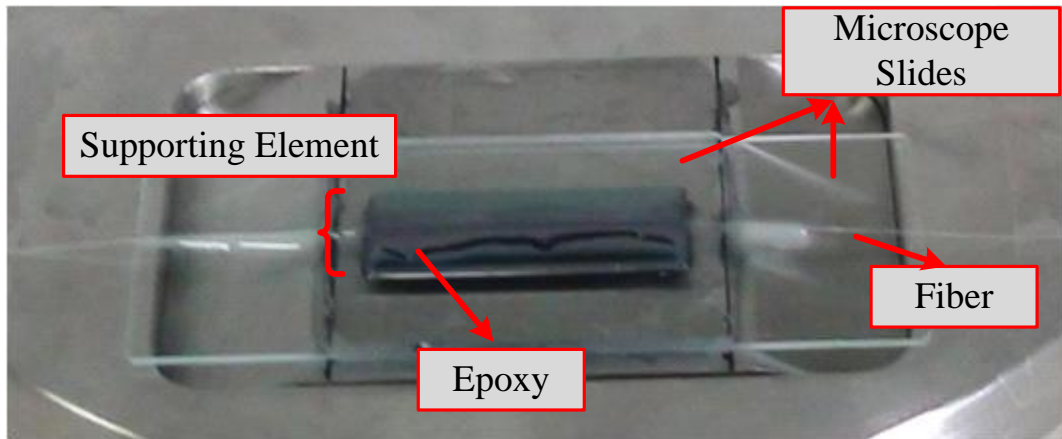


Figure 2.10 Placement of fiber into V-groove supporting element.

out with isopropyl alcohol to remove the polymer impurities. Also, supporting elements are rinsed with DI water, acetone, and isopropyl under microscope control. These cleaning processes prevent some imperfections on the fiber and inside the V-canals.

In order to fix unjacketed fibers into V grooves as in Figure 2.10, epoxy EPO-tek 301-1 (Epoxy Technology) is used as an adhesive. This epoxy is for optics, medical, and packaging of optical devices [80]. It consist two components and their mix ratio should be 20:5 by weight. Thus, the liquids are put on a glass container by using syringe with weighting and they are stirred slowly for 5 minutes. The adhesive is properly spread into V groove and the stripped portion of fiber is aligned into the canal with back and forth motions carefully. It is important to prevent occurrence of adhesive bubbles inside the grooves because their existence may cause scratches or cracks on fiber. Then, F/O cable is stretched in canals with sticky band to fix it until the epoxy is crystallized. Such an immobilization step is necessary to place the F/O cable in the V channel perfectly. Epoxy is cured at 30 °C on hot plate for a week.

2.3.2 Lapping and Polishing

Lapping and polishing processes' common purpose is to remove the material and reach the desired dimensions while having a smooth surface at the end of processes. These processes can be applied for metals, glasses, semiconductors, and ceramics.

The benefits of lapping and polishing techniques are being controllable and producing nanometer-scale flat surfaces [79].

The lapping and polishing protocol is implemented to cured F/O platforms with Struers (model: RotoPol 11) polishing machine. Various polishing steps are entailed to remove three different materials which are single crystal silicon, crystallized 301-1 epoxy, and silica fiber at the same time. Initially, a high material removal is provided with harder and coarser material SiC with a minimal damage to the surface. Lapping step produces dimensionally accurate specimen however smoothing surface requires finer abrasives. To eliminate surface defects 3 micron diamond and 0.04 micron silica abrasives are used. The mechanical properties of fiber, silicon, SiC, and diamond are given in Table 2.1 [70]. The fiber-placed supporting element is stick with wax (ATM-M, D-57636) on an aluminum slab to take of it easily. Waxes are characteristically plastic near room temperature but melt about 45 °C. The aluminum slab is heated and wax is spread on it. Then, supporting element is assembled on the slab and the system is cooled. SiC-2500 grit polishing pad is located on the polishing machine and the fiber is lapped for 10 minutes at 150 RPM. The rough material is removed with this step.

As a second step, polyurethane polishing pad is replaced instead of grit pad. 3 μm size diamond abrasive inside a water-oil based lubricant liquid is applied for 10 minutes at 150 RPM. Thus, the scratches occurred during first polishing step are mostly decreased. For final polishing step, polyurethane pad is used with 0.04 μm colloidal silica at 350 RPM to smooth rough surface of the device.

Table 2.1 Mechanical property of fiber, silicon, SiC, and diamond [70].

Materials	Hardness (kg/mm²)	Yield Strength (10¹⁰ dyne/cm²)	Young's Modulus (10¹² dyne/cm²)	Density (g/cm³)
Fiber (SiO ₂)	820	8.4	0.73	2.5
Si	850	7.0	1.9	2.3
SiC	2480	21	7.0	3.2
Diamond	7000	53	20.35	3.5

2.3.3 Mounting FC/PC Connectors

To provide a better light transmittance between fiber – laser and fiber – detector, FC/PC connectors are mounted on the fiber. This process begins with obtaining the required specific tools for multimode (50 μm core and 125 μm cladding diameter) fiber. The selected assembly tools are given in in section 2.1.

Optical connector elements (crimp sleeve, boot, and FC connector) are put into a beaker and the beaker is filled with isopropyl alcohol. After soaking them for five minutes, they are removed and dried. Then, fiber protective layer is stripped for 13 mm with stripping tool (Thorlabs, T08S13) and wiped with isopropanol. The fiber is placed into the boot, crimp sleeve, and FC connector as demonstrated in Figure 2.11.

Fixing fiber is provided by using a F112 model, 2-gram epoxy. The two-part epoxy locates inside a plastic package. They are mixed for one minute by rubbing the package on the edge of the table. After proper mixing the epoxy, it is loaded to the syringe (Thorlabs, MS403-10). Then syringe is inserted into the connector and epoxy is pressed till a small bead appears on the ferrule. The stripped fiber is slowly seated with back and forth motions into the FC connector. The crimp sleeve is slid to the FC connector from the back which is fixed with the 0.178 inch section of crimp tool (Thorlabs, CT042). Small amount of epoxy is added to the sleeve and the boot is placed on it. The assembled parts of connector with epoxy are cured for one day.

After the fiber and FC connector elements are united, the end section of fiber is needed to prepare with polishing steps. Firstly, the fiber connector is scored with fiber scribe (Thorlabs, S90W) just above the ferrule. Scoring step provides to cleave fiber edge properly. Secondly, FC connectorized fiber is inserted inside the polishing disk (Thorlabs, D50-xx). Then fiber edge is orderly polished with 5 μm , 3 μm , 1 μm , and 0.3 μm pads.

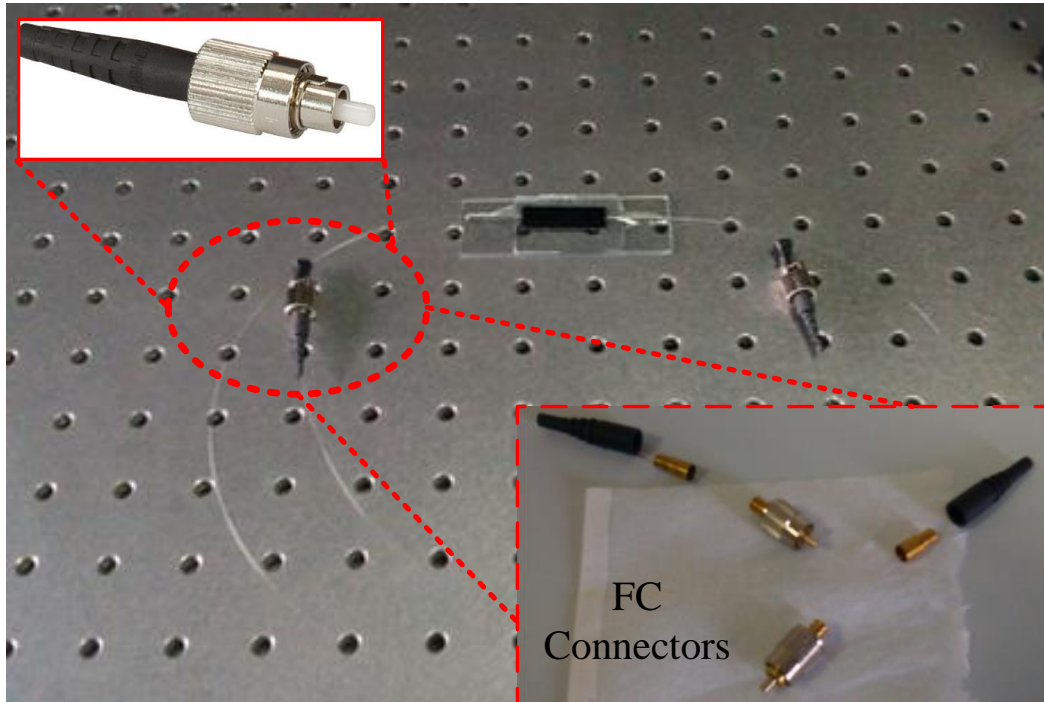


Figure 2.11 FC/PC connectors are joined with F/O sensor platform.

2.3.4 Sensor Surface Modification

Modifying physical properties of D-type F/O sensor surface provides us to enhance sensitivity for different RI regions. In this study, sensor sensitivity is increased with coating metallic thin film. Also, roughening film effect on the sensor sensitivity is studied in detail.

2.3.4.1 Thin Film Coating

In order to generate surface plasmon resonance and waveguide modes, gold thin film is coated to the differently deep polishing protocol applied sensors (Figure 2.12). Thin film coating processes can be divided into four general categories which are atomistic growth, particulate deposition, bulk coating, and surface modification [80]. Among the coating processes, atomistic growth with thermal evaporation system is more appropriate for the D-type F/O sensors because of lower temperature operation and usability of various heat sources. Thermal evaporation method deposits thin solid films by the condensation of a vaporized form of solid material onto various

surfaces. This system involves a chamber, vacuum pumps, source, refractory metal boat, and target material. In this study Vaksis model Thermal Evaporator (PVD Vapor - 3S Thermal) is used. First of all, the sources (Gold and Crom) are separately placed into Tungsten (W) metal boats; chamber is closed, and vacuumed. Then, Cr and Au are melted with heat and condensed onto the 5 mm middle portion sensor surface at 5×10^{-6} Torr pressure. Thus, 2 nm thickness Cr and 20 nm thickness Au are deposited to the surface, respectively.

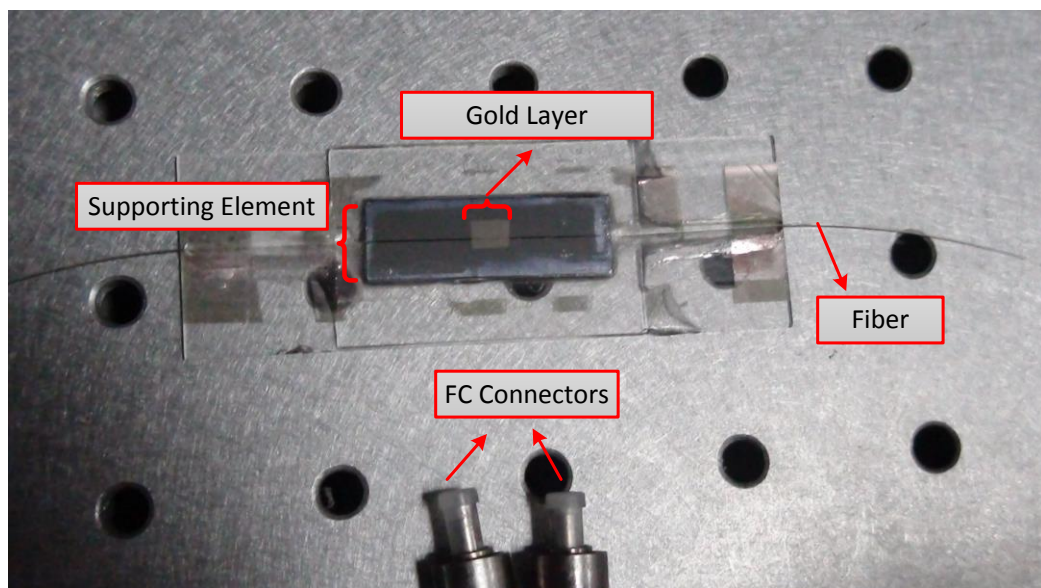


Figure 2.12 Thin film coated D-type F/O sensor.

2.3.4.2 RF Plasma Etching

Radio Frequency Plasma Asher/Etching is used to increase surface roughness of the gold film. This process is implemented with Argon (Ar) gas at 50 watt power and 5×10^{-2} mbar pressure for 2 and 4 minutes. Before application of plasma etching the chamber of system is cleaned by using Ar gas.

CHAPTER 3

CHARACTERIZATION

The characterization part of the thesis includes the analyzing results of supporting elements' fabrication, lapping and polishing protocol, and surface modification during experiments. Developing the waveguide (OWG) and surface plasmon resonance (SPR) modes based D-type F/O sensors with different polishing depths are provided by discussing the characterization results. Some major development parameters such as polishing depth, interaction length, and surface roughness are controlled with optical microscope, profilometer, and scanning probe microscope (SPM). These parameters monitoring and adjustment are very critical because the sensitivity of sensors depend on them.

3.1 Characterization of Supporting Elements

Handling F/O cable is provided with Si wafer supporting elements as discussed in section 2.2. Supporting elements are fabricated in four major steps which are mask production, lithography, buffered oxide etching (BOE), and potassium hydroxide etching (KOH). These processes are entailed directly to a 4-inch Si wafer. Then supporting elements are separated from each other with dicing saw machine. Because of supporting elements' production are maintained in the same processes, examining the grooving sections from different points is necessary. The width of grooving sections' mask and Si wafer are characterized with optical microscope (Leica-CTR6000) after lithography, BOE, and KOH processes as demonstrated in Figure 3.1.

Measuring the width of grooving section of mask and Si wafer allow us to determine how the designed pattern is changed with fabrication steps. The measurements are taken from the end region of grooves mostly because the widths are expected to be exact for grooves. In fact, the width narrows with approaching the middle parts of groove due to the design of mask. According to the obtained results given in Table 3.1, the width of grooves increases slightly by maintaining through the fabrication processes. It means mask should be designed at least about 10 μm smaller widths to produce grooves with desired dimensions.

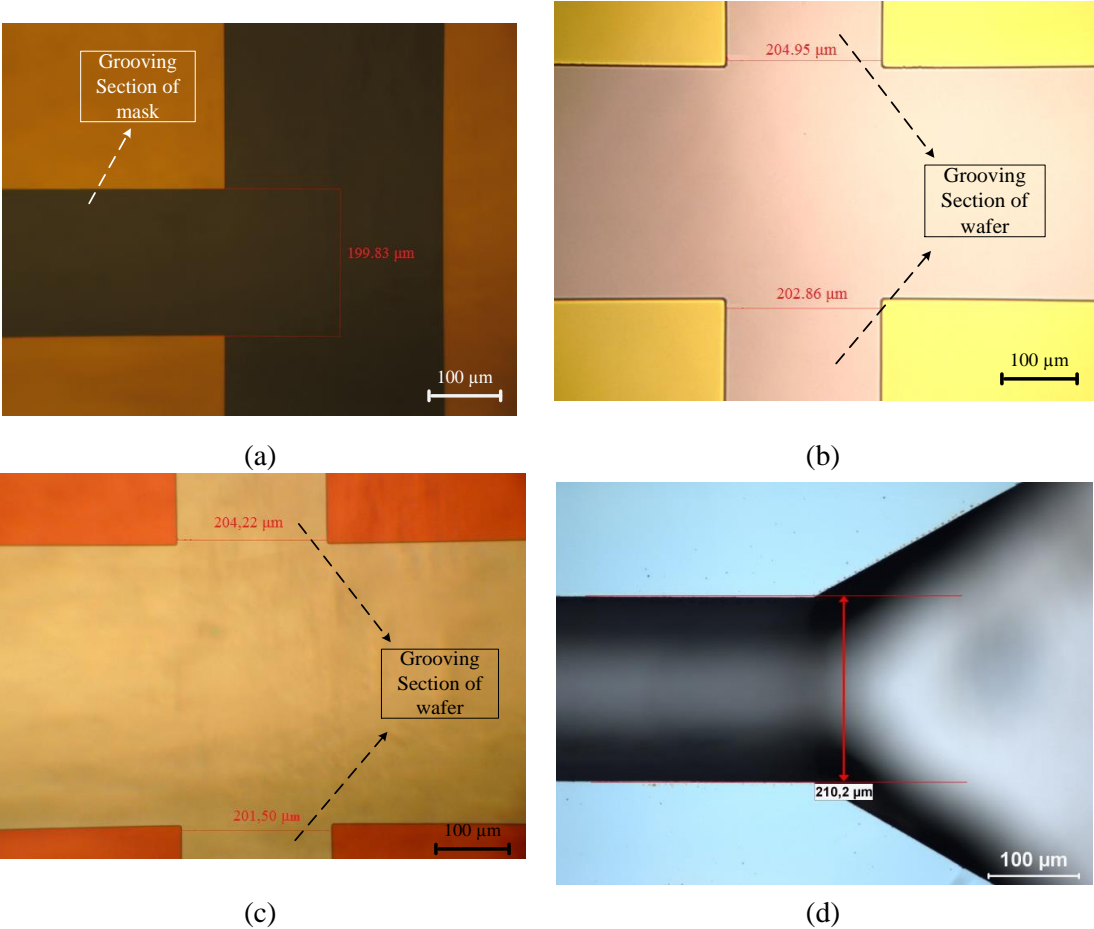


Figure 3.1 Microscope measurements of (a) mask, (b) lithography applied wafer, (c) BOE applied wafer, and (d) KOH etching applied wafer.

Table 3.1 Width measurements of grooves for each step.

Data	Mask	Lithography	BOE	KOH
1	196.91 μm	204.95 μm	204.22 μm	210.20 μm
2	197.12 μm	202.86 μm	200.46 μm	206.89 μm
3	198.32 μm	199.23 μm	201.50 μm	207.58 μm
4	197.95 μm	201.10 μm	201.30 μm	209.65 μm
5	198.58 μm	200.15 μm	201.50 μm	206.20 μm
6	199.62 μm	203.69 μm	201.50 μm	205.51 μm
7	197.74 μm	199.52 μm	204.22 μm	208.96 μm
Average	198.03 μm	201.64 μm	202.10 μm	207.48 μm

In order to monitor the depth of grooving section during BOE and KOH etching, Stylus Profilometer (KLA Tencor, P6 Surface Profiler) is used. The 9 minute buffered oxide etching application is removed about 5000 nm thickness oxide layer of silicon wafer. The profilometer measurements after BOE is presented in Figure 3.2 and the obtained data are given in Table 3.2.

The characterization results of profilometer measurements during KOH etching are presented in Figure 3.3 for different time durations between 30 minute and 300 minute. As the time passes, V-groove shape becomes more significant. This process is completed in 345 minute with 25 micron/hour rate. The deep measurements are given in Table 3.2 after KOH etching process is completed.

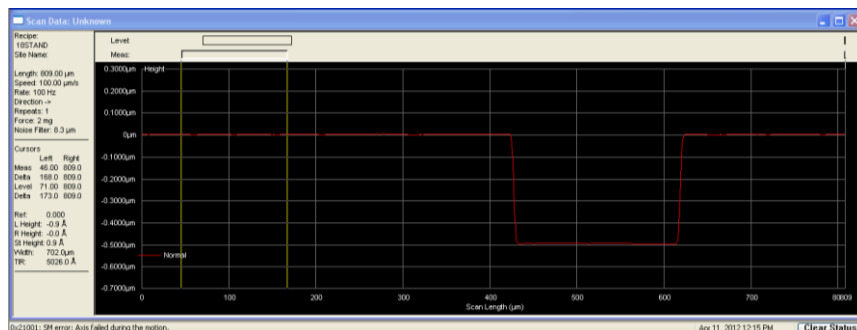
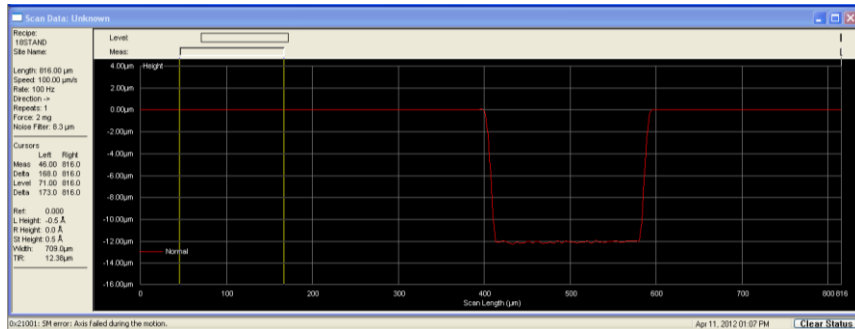


Figure 3.2 Profilometer measurements after buffered oxide etching (BOE).

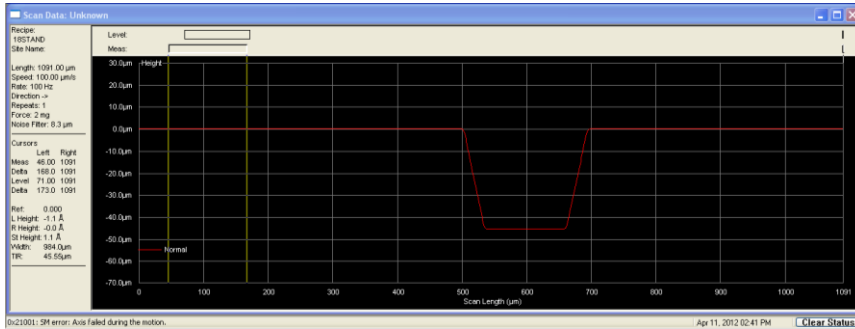
The depths of middle and end region of supporting elements are different due to the narrowing design of grooves. There is approximately 10 μm depth difference inside the V-groove supporting elements.

Table 3.2 Depth measurements after BOE and KOH.

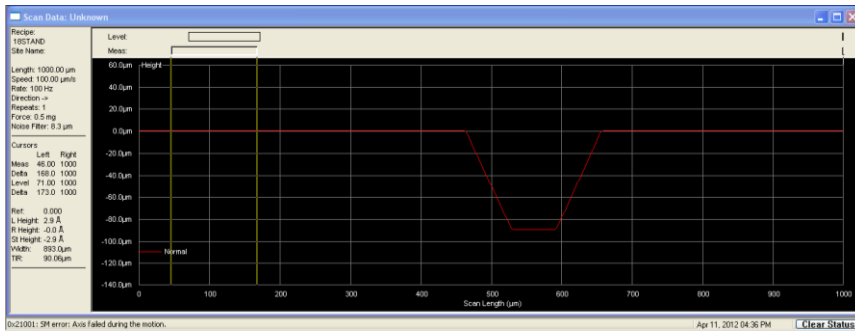
DATA:	1	2	3	4	5	6	Average
Buffered Oxide Etching (BOE) (μm)	0.498	0.497	0.499	0.501	0.503	0.500	0.4997
Potassium Hydroxide Etching (KOH) (μm)							
Ends	146	147	145	148	143	140	144.8
Middle	135	137	134	136	135	133	135.0



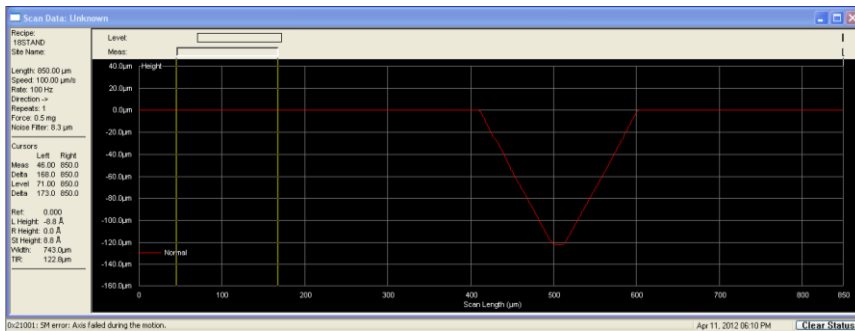
(a)



(b)



(c)



(d)

Figure 3.3 Profilometer measurements during KOH etching for (a) 30 min., (b) 100 min., (c) 180 min., and (d) 300 min.

3.2 Analyzing Lapping and Polishing Protocol

To expose the core region of the F/O, we remove materials with various lapping and polishing steps as mentioned in section 2.3.2. After each lapping and polishing step, transducer (F/O placed into the supporting element) should be examined to understand whether the lapping & polishing steps are applied properly. Indeed, we have to deal with many problems during the application of protocol such as nonlinear polishing surface or fiber breakage. Also, the polishing depth and interaction length of produced F/O sensors are determined with measuring the V-groove width.

The polishing depth (h) as shown in Figure 3.4 which is distance from the core-cladding interface to the polishing surface defines the polishing depth of the F/O sensor. Depth of V-groove has a relation with crystal orientation angle ($\alpha_2 = 54.7^\circ$, between (100) and (111) planes), fiber core and cladding radius as given in equation 3.1.

$$\begin{aligned} d_h &= R/\sin(\alpha_2) + r & h &= 0 \\ d_h &> R/\sin(\alpha_2) + r & h &> 0 \\ d_h &< R/\sin(\alpha_2) + r & h &< 0 \end{aligned} \quad (\text{eq. 3.1})$$

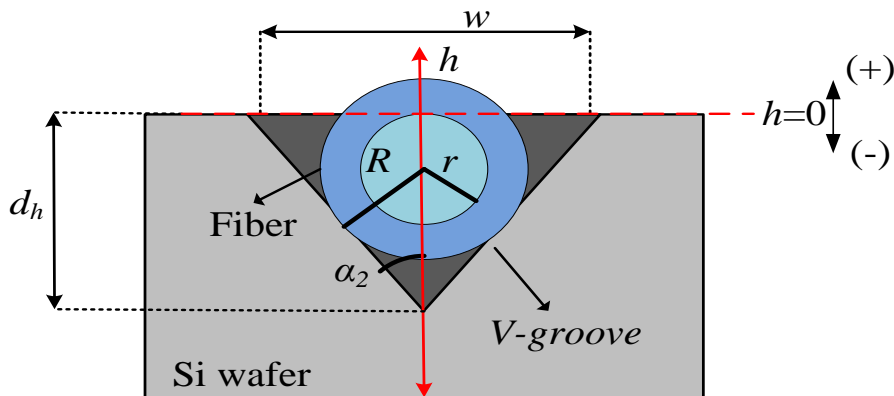


Figure 3.4 Front view of the polished fiber inside the V-groove. The dimensions are d_h = depth of V-groove for the edge of core and cladding region, α_2 = crystal orientation angle, h = polishing depth, R = fiber radius, and r = fiber core radius.

Besides the polishing depth of F/O sensor, it is also necessary to analyze the parameter of interaction length. The polished region of fiber provides interaction between sensor system and external media. Molecular level changes inside the external media alter the light intensity of sensor system so measurements become applicable. The interaction length of fiber as shown in Figure 3.5 can be enlarged with increasing polishing depth.

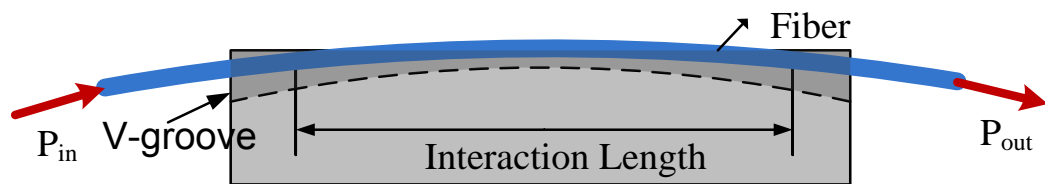


Figure 3.5 Side view of the polished fiber inside the V-groove.

By using lapping and polishing procedure, sensors are produced at four different polishing depths ($h = +5$, $h = -5$, $h = -10$, and $h = -20$). These transducers are examined with optical microscope (Leica, model: DFC320) at 20X and 50X magnifications after each lapping & polishing steps as given in Figure 3.6 – 3.9. After the first lapping step with 9 μm pad, many scratches and faults are observed on the fiber surface. However, they are removed and polished with the second (3 micron diamond) and third polishing steps (0.04 micron colloidal silica).

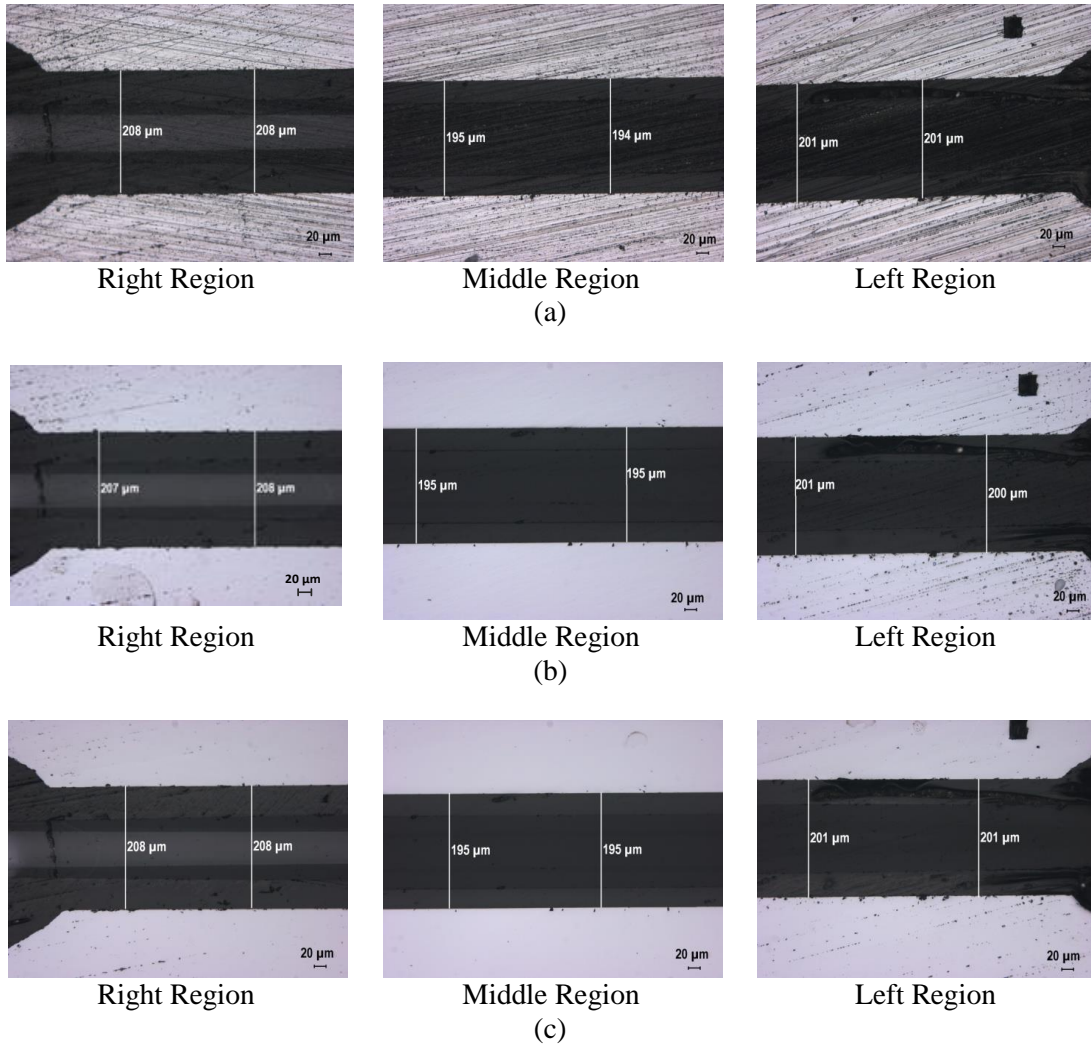


Figure 3.6 Optical microscope measurements of (+5) polishing depth sensor after (a) 9 μm pad, (b) 3 μm diamond, and (d) 0.04 μm colloidal silica.

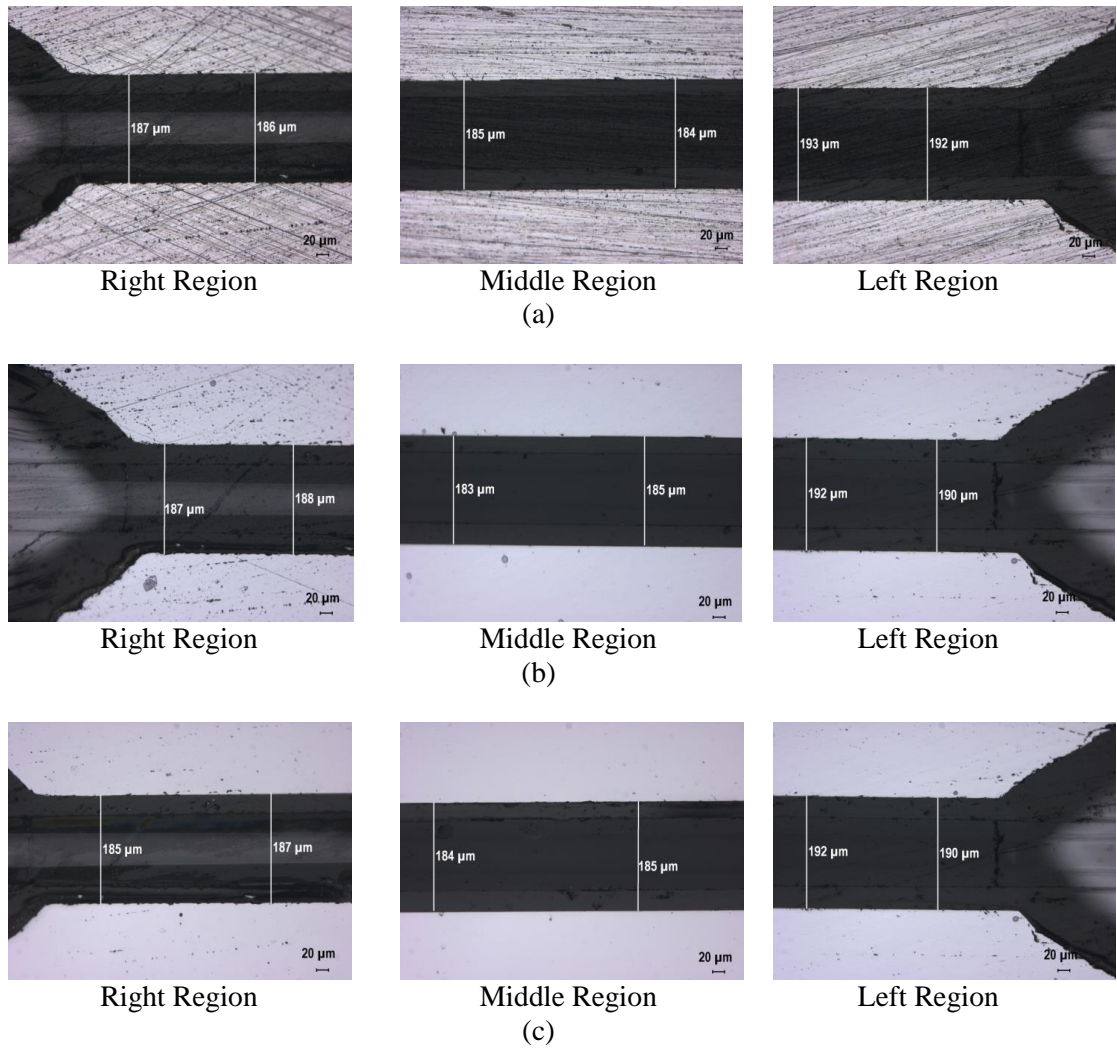
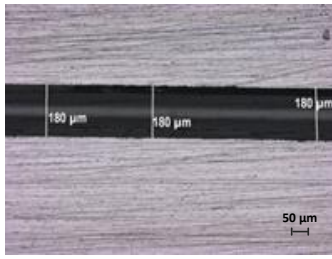


Figure 3.7 Optical microscope measurements of (-5) polishing depth sensor after (a) 9 μm pad, (b) 3 μm diamond, and (d) 0.04 μm colloidal silica.



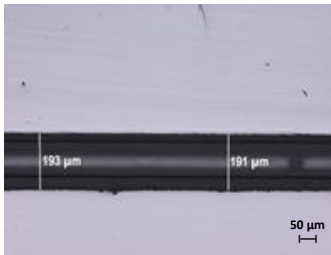
Right Region



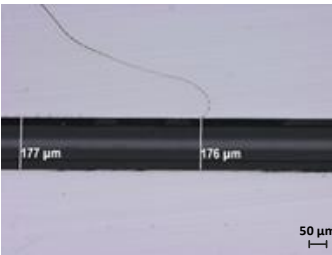
Middle Region
(a)



Left Region



Right Region



Middle Region
(b)



Left Region



Right Region



Middle Region
(c)



Left Region

Figure 3.8 Optical microscope measurements of (-10) polishing depth sensor after (a) 9 μm pad, (b) 3 μm diamond, and (d) 0.04 μm colloidal silica.

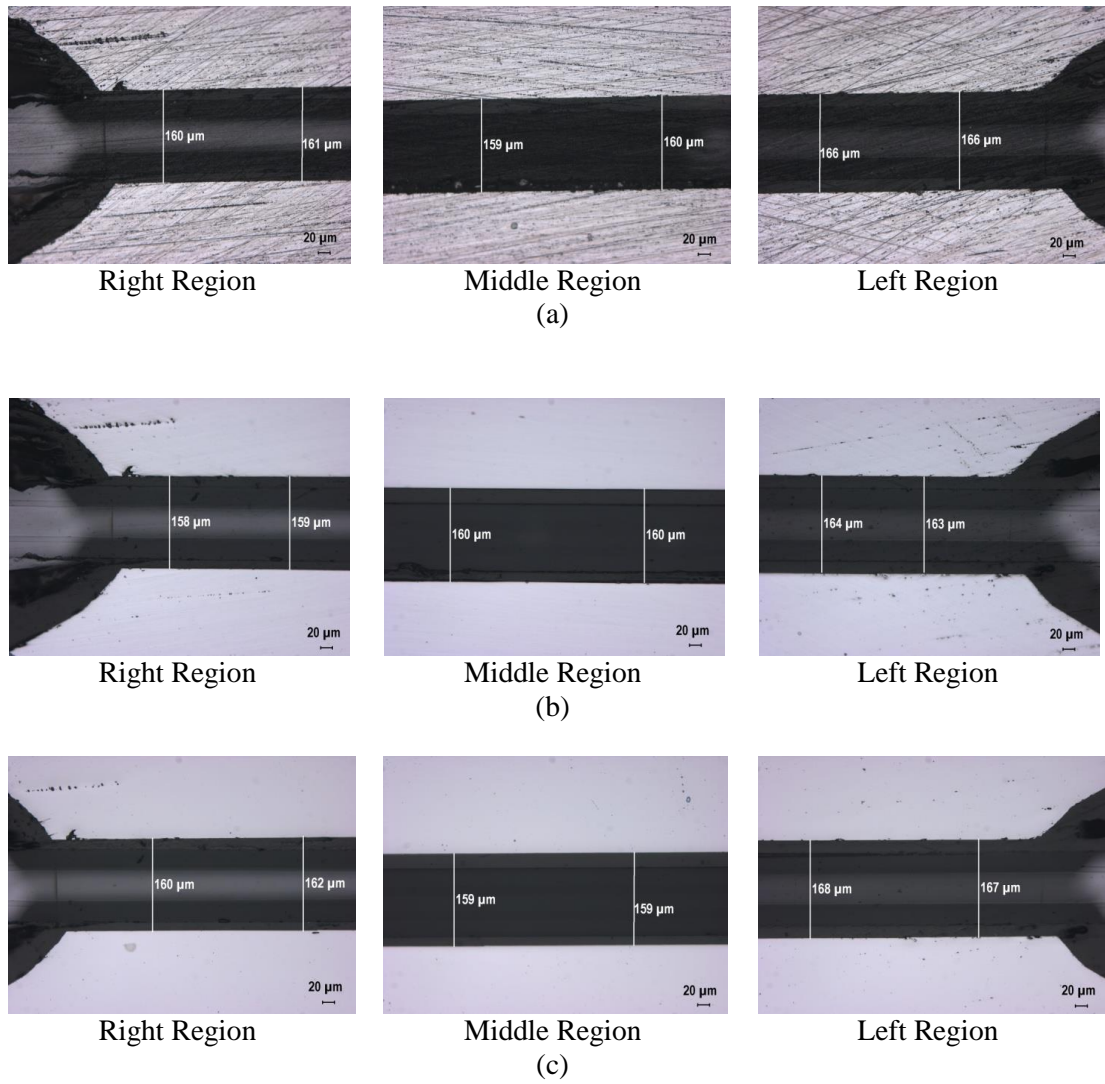


Figure 3.9 Optical microscope measurements of (-20) polishing depth sensor after (a) 9 μm pad, (b) 3 μm diamond, and (d) 0.04 μm colloidal silica.

After the third polishing step, the roughness of platforms are measured approximately 1.40 nm using Scanning Probe Microscope (SPM) (QuesantAmbios Universal) with 40 μm scanning head at 1 Hz scan rate in contact mode that separation power 6 \AA X and Y, 0.5 \AA Z directions is shown in Figure 3.10.

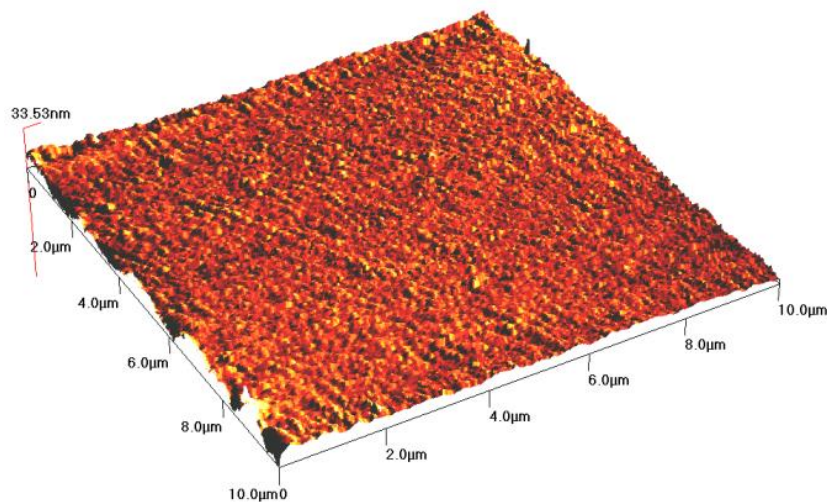
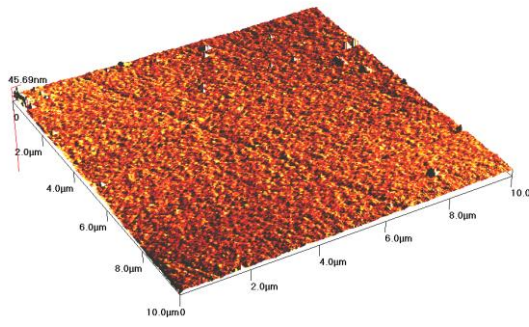


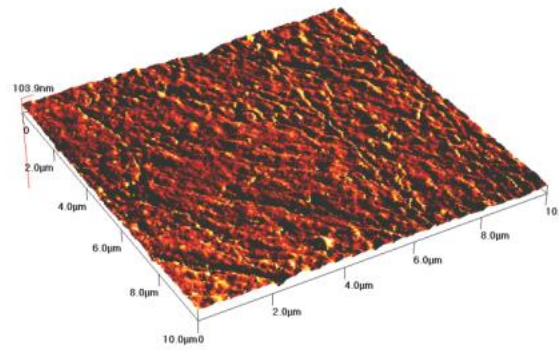
Figure 3.10 SPM roughness image of the fiber's polished surface (1.40 nm).

3.3 Surface Modification

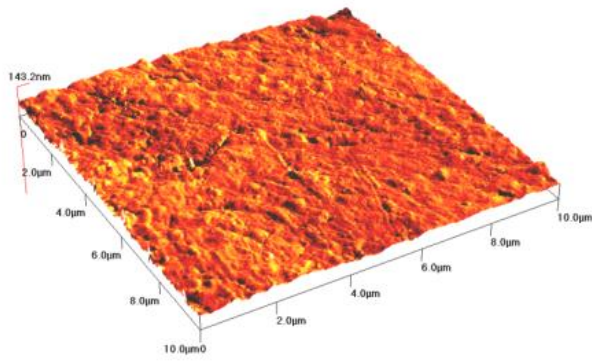
We modified sensor surface to increase the sensitivity of sensor by coating thin gold film and roughening the sensor surface. It is known that depositing thin metallic film excites SPR mode. Thus, we coated thin gold film to the different polishing depth applied transducers' surfaces. Then, RF plasma etching is applied to rough the surface. This process is resulted in gold nanoparticles with different sizes. Their shapes and sizes can shift the plasmonic mode [81]. After the each process, the surface of transducers are characterize with SPM. The measured roughness values are 3.0 nm, 5.6 nm, and 7.8 nm for 0, 2, and 4 min. of plasma etchings respectively as demonstrated in Figure 3.11.



(a) Ra= 2.99 nm



(b) Ra= 5.63 nm



(c) Ra= 7.82 nm

Figure 3.11 Scanning Probe Microscope (SPM) images of Au coated sensors of roughness (a) w/o, (b) 2 min., and (c) 4 min. plasma etching process.

CHAPTER 4

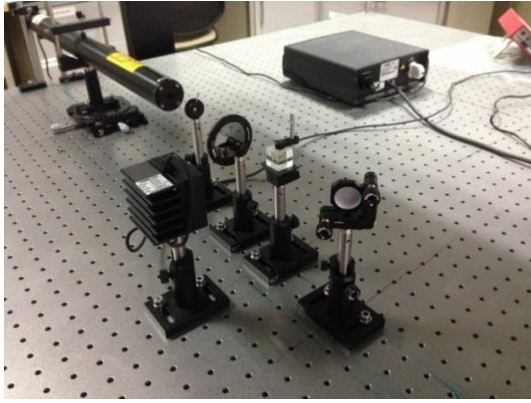
TESTS AND MEASUREMENTS

4.1 Measurement System

Opto-mechanical measurement set up is designed and built on an optical table(Newport, ST). It includes laser system, iris, filter, beam splitter, mirror, x-y-z stage fiber controllers and detector components as seen in Figure 4.1 and Figure 4.2. All of the equipment is purchased from Thorlabs.

As power generator, three different linearly polarized He-Ne laser systems are used. They generate light at 543nm (Thorlabs, model: HGR005), 594nm (Thorlabs, model: HYP020), and 632.8 nm (Thorlabs, model: HNL150R) wavelengths. For measurements, mostly used the 632.8 nm in the red portion of the visible spectrum laser generates 25 mW powers with 0.5% RMS noise. Furthermore, 543 nm (green) and 594 nm (orange) wavelength laser systems produce 0.5 mW and 5 mW orderly with 1% RMS noise. The cylindrical laser head is mounted in V-clamp blocks to stabilize on optical table. The linearity is provided with positioning stage and iris.

The released light from laser is divided into two beams by using an unpolarizing Cube Beamsplitter in that taking reference measurements with a detector (Thorlabs, model: S310C) continually is necessary. The reference measurement allows decreasing the noise generated from the lasers. The other beam is oriented with mirror through the x-y-z stage (Thorlabs, model: MBT613D/M). This stage controls F/O cable and let the light enter through the FC connector.



(a)



(b)



(c)



(d)

Figure 4.1 Opto-mechanical measurement system images (a), (b), (c), and (d) are taken from different views.

Some portion of the light is coupled into the fiber with an x-y-z translation stage.. The F/O cable is a waveguide and light can propagate through it with total internal reflection principle. When the light passes through the interaction area of the F/O sensor head, its intensity changes due to the processing applied to the sensor's surface as mentioned in Section II. The difference between the light amounts entering and exiting the F/O cable is measured with two detectors (Thorlabs, model:

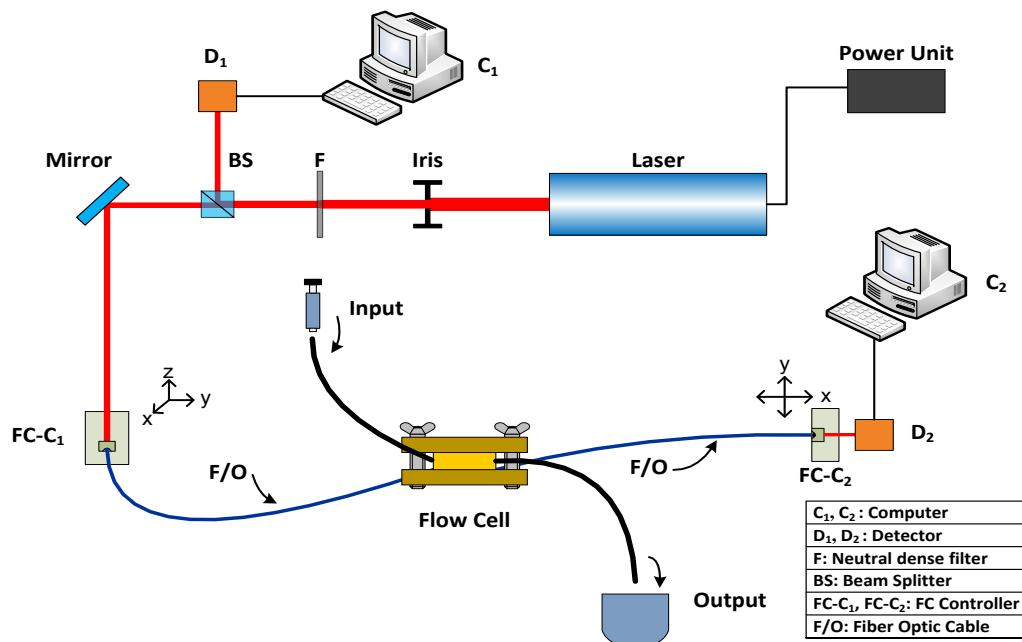


Figure 4.2 Measurement system schematic views.

PM121D). The detectors and fiber FC/PC connector is stabilized and aligned with the x-y-z stages.

The flow cell section includes syringe, 3 mm diameter and 15 cm long two Teflon cables, preformed rubber seal, flow cell head, and beaker. The flow cell head is designed for liquid flow through the sensitive region of sensor. It is fabricated with “Teflon” material about 2 mL volume. Furthermore, its dimensions are carefully determined in design step as illustrated in Figure 4.3 because solutions being on the surface of sensor needs to contact perfectly and also, formation of air bubbles should be prevented. The flow cell head special design is presented in Appendix C. The flow cell head is connected with Teflon cables from two end sides. Input and output of liquids are provided with these cables. Input cable is mounted with a syringe tip by using an epoxy (Thorlabs, G14250) being crystallized in 5 minutes, thus syringe can be used easily with the assembled tip inside the cable. Output cable end side is placed into a beaker to get rid of the waste solution.

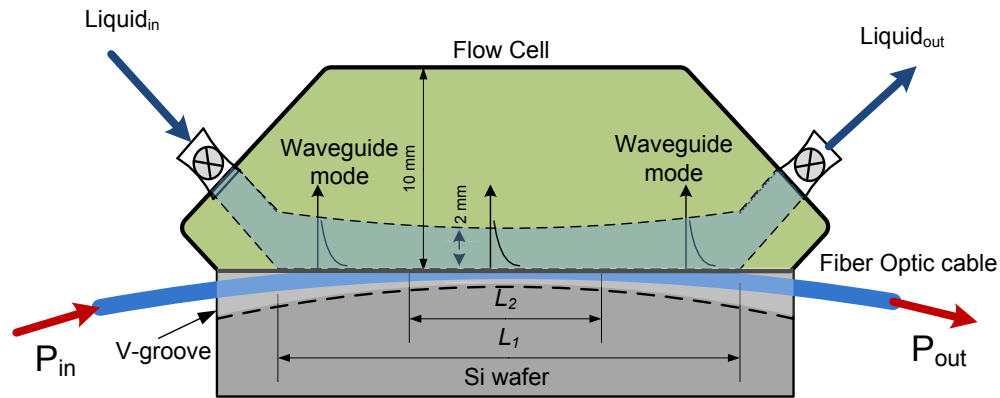


Figure 4.3 Flow cell attached to the F/O sensor head (side view).

4.2 Preparation of Solutions

In order to carry out measurements with developed D-type F/O sensors, different RI liquids are used. As liquids varied concentration glycerin-water mixtures and IgG proteins hindered aqueous solutions are preferred to assembly on polished side of fiber by utilizing a flow cell.

Main aim of Glycerin-water measurements is to determine the behavior of produced sensors. When the concentration of glycerin-water mixture is changed, the RI of solutions varies [5]. These mixtures have three important advantages which are the wide range refractive indices, the ability of mixing easily, and being chemically not attractive. Therefore, glycerin-water solutions at different concentrations are preferred to characterize sensors.

The basic principle of biological experiments is that measuring the combination of a specific antibody and antigen complex as demonstrated in Figure 4.4. An antibody is an immunoglobulin ability to bind both the antigen and surface of system [6]. Y-shaped antibodies have two arms to let antigen binding and a constant Fc tail which serves as linking with system. On the other hand, antigen such as proteins, lipids, or

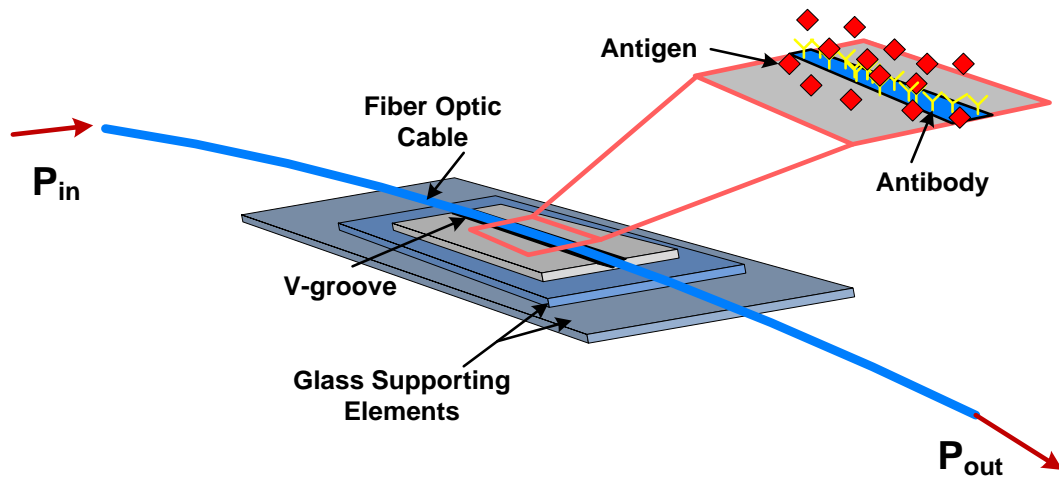


Figure 4.4 Antibody and antigen combination on the d-type F/O sensor.

nucleic acids is able to chemically combine with the specific antibodies [7]. Antibody and antigen interactions rely on hydrogen bonds, hydrophobic interactions, or forces such as electrostatic or van der Waals [8]. The nature of interactions depends on the association of antibody and antigen complex

4.2.1 Glycerin-Water Solutions

Glycerin is purchased from Merck with 99.5% purity being used for measurements at different concentrations. The illustrated chemical structure of Glycerin ($C_3H_8O_3$) in Figure 4.5, molecular weight is 92.09 g/mole and RI is 1.47 RIU [9]. The three hydroxyl group in glycerin makes it miscible in water. Therefore, it is possible to prepare different RI solutions via the wide range refractive indices between 1.33 RIU and 1.47 RIU intervals with variant glycerin concentrations in water. There is a linear relationship between glycerin-water concentration and RI at 25 °C being presented in Equation 4.5 and Figure 4.6 [10].

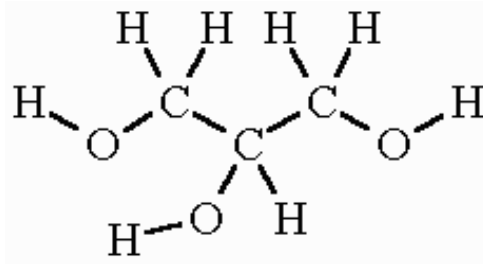


Figure 4.5 The chemical structure of Glycerin [11].

$$n_s = 1.4638 + 0.00146(C - 95) \quad (\text{eq. 4.5})$$

In this way, 20 liquid samples are independently prepared in distilled Millipore water. Glycerin and water mixtures are scaled and 50 mL solutions are prepared with different concentrations for measurement. Each liquid stirred fifteen minutes with magnetic mixer. This process causes some bubbles inside the solutions so it is necessary to wait for one day at the room temperature before measurements.

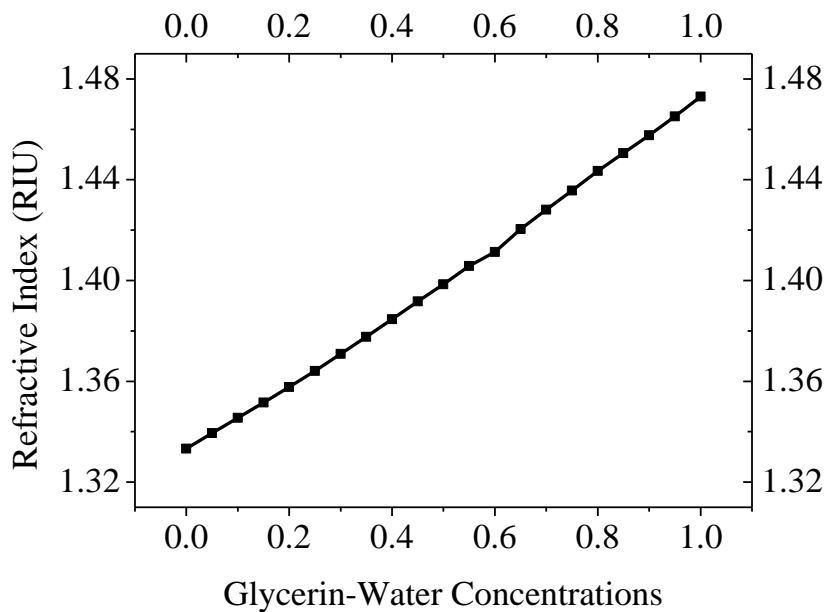


Figure 4.6 RI and glycerin-water concentrations relationship.

4.2.2 Biological Solutions

It is possible to measure biological solutions such as proteins in liquid with the developed d-type F/O sensors. Therefore, to perform protein detection IgG proteins are used. As antibody reagent Rabbit Anti-Mouse IgG (RAM) is used while as antigen reagent Mouse IgG (MIgG) protein is selected and they are purchased from Jackson Immuno Research Laboratories Inc. ChromePureMIgG proteins concentration is 5 mg/mL in sterile filtered phosphate buffer liquid. On the other hand, Affini Pure MIgG, Fc_γ antibody has 2.3 mg/mL concentration which is purified from antisera by immune affinity chromatography using antigens coupled to agarose beads. Both RAM and MIgG proteins are stored at 4 °C under sterile conditions.

In order to prepare proteins at different concentrations specifically developed Phosphate Buffered Saline (PBS) for the usage of immunoassay procedures in tablet form is obtained from Sigma Aldrich. One tablet PBS is dissolved in 200 mL of distilled water with magnetic stirrer for 15 minutes at 600 RPM. The prepared liquid has 0.01 M phosphate buffer, 0.0027 M potassium chloride, and 0.137 M sodium chloride with pH 7.4 at 25 °C. The solution is filtered with vacuum filtration unit (Isolab) by using membrane.

The concentrations of Rabbit Anti-Mouse IgG and Mouse IgG proteins are firstly decreased to 5 μg/μL. The solution is divided into 500 μl and inserted to 1000 μl-tubes (Eppendorf) with proper mixing. These prepared solutions are freezed at -22 °C to use as stock because solutions must be ready for daily measurements otherwise proteins die.

4.3 Sensitivity Measurements

The experiments are performed with Opto-mechanical measurement set up system and prepared solutions. Firstly, mounted laser in measurement system is started to work and waited half an hour to provide stable optical outputs. Once the laser warm up, the needed arrangements for optical system are carried on with the experimental system control. Before taking measurements, flow cell is cleaned with 5 mL ethanol and 5 mg DI water by using syringe to remove impurities. This procedure is repeated

for three times. Then, sensor is placed into flow cell and this configuration is assembled with optical system.

For the glycerin-water liquid experiments, sensitive region of D-type F/O sensor is rinsed with DI water and isopropyl for 5 minutes. The flow cell is filled with prepared solutions by one by one and after each solution DI water is syringed into flow cell to reach the initial status of the sensor. Data are taken regularly from detector systems every 30 seconds after the liquid samples syringed to the flow cell.

For the biological measurements, sensor surface is cleaned with DI water and isopropyl for 5 minutes and plasma etching is applied for 1 minute at 50 watt power as mentioned in section 2.3.1. Sensor is placed into measurement system as soon as possible after plasma etching and 15 mL PBS is syringed into the flow cell to be sure the surface of sensor is clean. The prepared stock solutions of RAM and MIgG at -22 °C described in section 3.2.2 is melted. Firstly, 1 mL RAM and 5 mL PBS is assembled into flow cell which is repeated two times. To observe antibody-antigen connection 50 µg/µL concentration MIgG is assembled about 2 mL, then 5 mL PBS is syringed.

4.4 Temperature Measurements

The developed different polishing depth d-type F/O sensors sensitivity measurements with respect to change of temperatures are entailed between 23 °C and 30 °C ranges. The used solution in experiment is a mixture of water (25%) and glycerin (75%) solution having the thermo-optic coefficient is about -10^{-4} K^{-1} at 25 °C [14 and 15]. Besides, fiber core and cladding thermo-optic coefficient is $dn_{\text{core}}/dT \approx dn_{\text{cladding}}/dT \approx -10^{-4} \text{ K}^{-1}$ at 25 °C, which is too small to detect during measurement [12]. Thus, the changes in fiber are negligible and this gives a chance to detect only the solution of RI difference. A linear output power and temperature relation is obtained fitting with the negative thermo-optic coefficient variation.

Before doing experiments, measurement system is changed to carry on temperature analyses. A hot plate (IKA, RCT standard) is placed under the flow cell and needed

mechanical arrangements are entailed for the system. Also, a thermometer is touched near the sensitive region of sensor to be sure the exact temperature is reached.

For temperature measurement experiment flow cell is cleaned three times with ethanol and distilled water. The properly wiped out sensors with isopropyl and DI water are assembled to measurement system one by one. The prepared 1.43 RIU solution at 25 °C is syringed into flow cell and data are monitored from 23 °C to 30 °C with 1 °C range. The measurements are carried on in 15 minutes.

4.5 Wavelength Measurements

For the wavelength measurements, three different laser systems at 543 nm, 594 nm, and 633 nm wavelengths are used to detect the wavelength effect. Glycerin-water solutions between 1.33 RIU and 1.47 RIU ranges are entailed to -10 μm polishing depth sensor with three lasers as mentioned in section 3.3.

CHAPTER 5

RESULTS AND DISCUSSION

In this section of the thesis, the obtained results from opto-mechanical measurement system are discussed. Initially, the typical behavior of sensors is presented for a wide range of RI interval between 1.32 and 1.47. Results indicate that the sensor response in three different RI ranges zones (I: 1.32-1.44, II: 1.44-1.46, III: 1.46-1.47) can be improved by the polishing depth. A maximum sensitivity 2×10^5 for the D-type F/O sensors is demonstrated in the RI range of 1.44-1.46. For biological measurements, zone I (1.32-1.44) is the most important RI interval. To increase the sensitivity of sensor around this zone, D-type F/O sensors' surfaces are modified by coating gold thin film and roughening. These two major modifications are used to control surface plasmon (SPR) and waveguide (OWG) surface modes. Thus, sensitivity of sensor is increased between 1.32-1.44 RIs by adjusting surface plasmon (SPR) and waveguide (OWG) modes' amplitude and resonance points. Additionally, molecular interaction measurements are carried on to demonstrate whether the developed D- type F/O sensors could detect molecular bindings on the gold surface. Interaction of IgG-protein molecules are detected with label-free and on-line measurements.

5.1 Typical Behavior of the D-type F/O sensor

To determine the D-type F/O sensor typical characteristics, both the output and the input powers are measured as a function of the time with the -10 μm polished sensor. The responses of the sensor to refractive indices 1.38, 1.41, 1.44, 1.45, 1.46, and 1.47, corresponding to glycerin concentrations of 40, 60, 80, 85, 91, and 100 wt. %

respectively are shown in Figure 5.1 (a). The higher solution concentration makes the output power decreases. The 1.46 RIU solutions does not even allow the light passing through the fiber because the bio-layer RI reaches to the fiber core RI (1.46). In the experiment, the water with 1.33 RIU can be used as a reference between each RI measurement. Thus, it is observed that the sensor is capable for continuous sensing in real-time. Furthermore, in Figure 5.1 (b) the output power change versus the RI variation is presented. Solutions with 20 different refractive indices are used for measurements. According to the graph three different RI zones (I: 1.32-1.44, II: 1.44-1.46, III: 1.46-1.47) are defined. Increasing RI of solutions decreases the output power slowly in the first zone and sharply in the second zone but, the output power increases slightly in the third zone.

In order to understand polishing depth effects (h) on sensor response, the F/O sensors with +5 μm , -5 μm , -10 μm and -20 μm polishing depths are fabricated and examined with measuring both the output and the input powers as a function of varying the refractive indices on the bio-layer as illustrated in Figure 5.2. When the RI varies between 1.33 and 1.48, the polishing depth does not affect the characteristic of the sensor response.

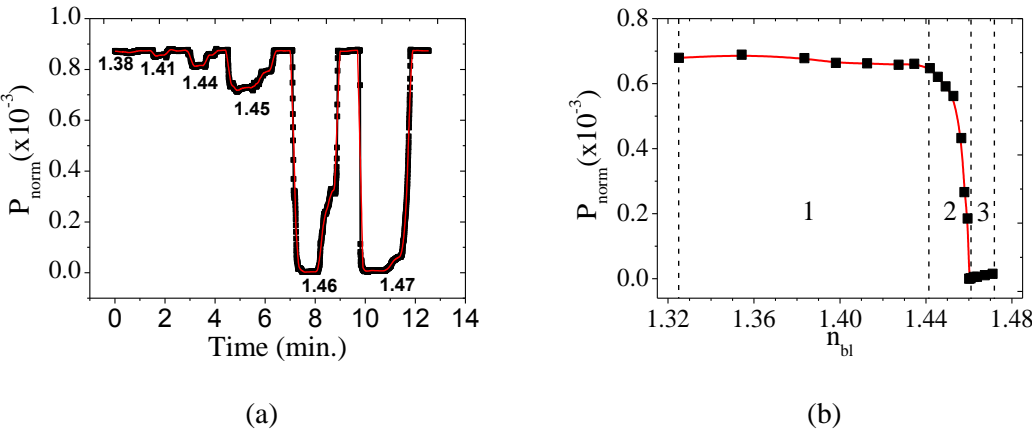


Figure 5.1 Typical OWG sensor behavior: (a) Time response and (b) zones for the refractive index changes.

Figure 5.3 indicates that the average output power changes as a function of the polishing depth in zone I. There is only amplitude change on the output power with the decreasing polishing depth because of the increasing loss.

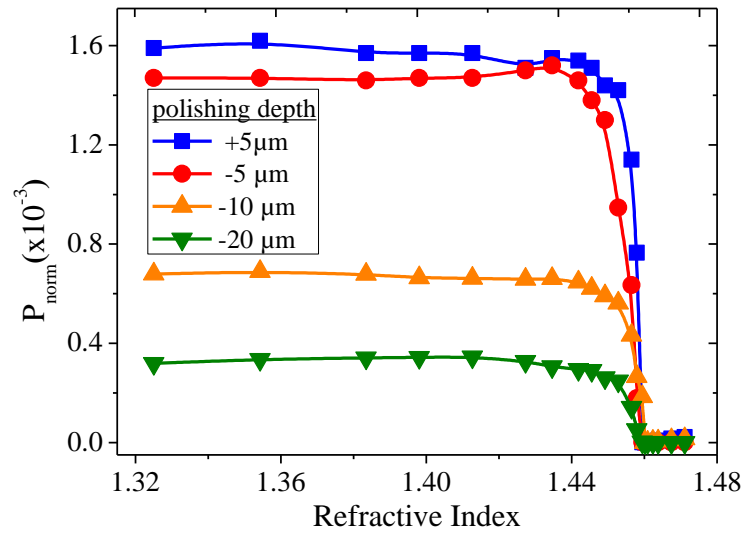


Figure 5.2 Effect of the polishing depth on the response of the D-type F/O sensor.

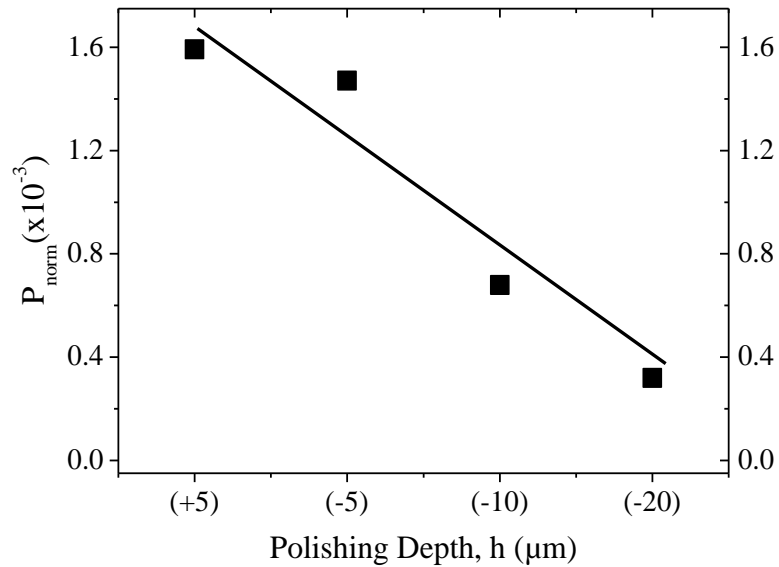


Figure 5.3 Graph of average output power in zone I vs. the polishing depth.

The D-type F/O sensor performance can be defined with a sensitivity parameter that is the indication of how good sensor's response to the less amount of molecular concentrations. This performance parameter is capable of explaining the levels of physical parameters' effects on output of the sensor. If there is no mechanical stress change during measurements, the sensor's sensitivity can be written as shifts inside the bio-layer.

$$S = \frac{\delta P_{norm}}{\delta n} + \frac{\delta P_{norm}}{\delta T} \quad (\text{eq. 5.1})$$

$$\delta P_{norm} = \frac{\delta P_{out}}{\delta P_{in}} \quad (\text{eq. 5.2})$$

Where δn is the RI change, δT is the temperature change, δP_{out} is the output power difference, δP_{in} is the input power difference, and δP_{norm} is the normalized power. Decreasing polishing depth allows us approaching the higher intense EM modes. They have strong evanescent wave tail so it is possible to increase the sensitivity of the sensor by modifying effective mode on evanescent wave. Therefore, sensitivities of the +5 μm , -5 μm , -10 μm and -20 μm deep polished sensors are examined at $\lambda = 633 \text{ nm}$ at 25 °C. The sensitivities are calculated and presented in Table 5.1 according to the three RI zones.

For the first RI zone (1.33 - 1.44), decreasing polishing depth increases the sensitivity of sensors till -10 μm height. However, the -20 μm deep sensor cannot detect the RI differences as the -10 μm sensor. This result reveals that sensors' sensitivity can be enhanced with the decreasing polishing depth. However the power loss should not exceed the needed power limit as the -20 μm deep polished sensor. For the second zone (1.44 - 1.46), decreasing polishing depth decreases the sensitivity. Although polishing through the fiber core allows reaching higher intense modes, the best molecular detection measurements are possible in the range of 1.44-1.46. The power loss effect is more influential in the second zone. For the third zone (1.46 - 1.47), there is no relation between the polishing depth and the sensitivity. Each sensor has its own characteristic sensitivity for the third region. Besides, among these three regions best sensitivity is obtained in the second zone because of the fiber properties. The refractive index of the fiber core is 1.46 and fiber cladding is 1.44 respectively. Thus, sensor sensitivity has a dramatic change in the second zone.

Table 5.1 Sensitivities of the D-type F/O sensors for different polishing depths.

Wavelength	Temperature	Polishing Depth, h (μm)	Zone	RI Ranges	Sensitivity ($\delta P_{\text{norm}}/\delta n$)
633 nm	25 °C	+5	I	1.3251 - 1.4419	1070.7
			II	1.4419 - 1.4601	197628.5
			III	1.4601 - 1.4711	4739.3
		-5	I	1.3251 - 1.4419	1095.3
			II	1.4419 - 1.4601	187265.9
			III	1.4601 - 1.4711	26.4
		-10	I	1.3251 - 1.4419	1113.6
			II	1.4419 - 1.4601	83333.3
			III	1.4601 - 1.4711	3205.1
		-20	I	1.3251 - 1.4419	471.7
			II	1.4419 - 1.4601	37878.8
			III	1.4601 - 1.4711	6.3

The best polishing depth changes depending on the RI zone. It is necessary to select an appropriate polishing depth during fabrication process because sensitivities scale up or down depending on RI zones. Also, the power loss with the polishing should be taken in consideration.

5.2 Wavelength Measurements

Figure 5.4 illustrates the wavelength effects being examined with the relative power ratio as a function of the refractive indices on the bio-layer with the -10 μm deep sensor. To obtain data between $n = 1.33$ and 1.47 three laser are used with 543nm, 594nm and 633nm wavelengths. Remarkably, the wavelength difference does not affect sensor's output power and its variation considerably but, sensor RI zone is shift a little bit. The best sensitivity is obtained with the 633nm laser.

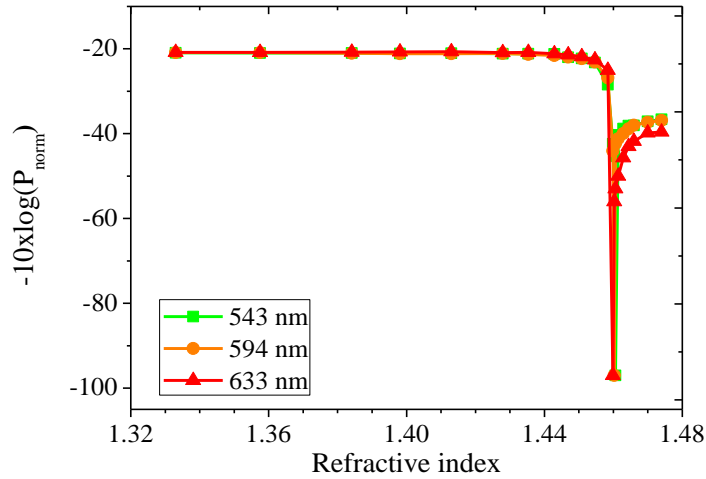


Figure 5.4 The wavelength effect on the sensor's response.

5.3 Temperature Measurements

The eq. 3.1 indicates that sensor's response depends on both RI and temperature variations. Therefore it is important to investigate sensor's temperature response in order to get more accurate RI measurements. The RI changes with respect to thermo-optic coefficient of materials (see the second term in eq. 3.1). In this way, the effect of the temperature on the sensitivity of +5 μm , -5 μm , -10 μm and -20 μm deep polished sensors is analyzed between the ranges 23°C to 30°C, as shown in Figure 5.5. The used solution in experiment is a mixture of water (25%) and glycerin (75%) solutions having the thermo-optic coefficient is about -10^{-4} K^{-1} at 25°C [12, 13]. Besides, fiber core and cladding thermo-optic coefficient is $dn_{\text{core}}/dT \approx dn_{\text{cladding}}/dT \approx -10^{-6} \text{ K}^{-1}$ at 25 °C, which is too small to detect during the measurements [14]. Thus, the changes in fiber are negligible and this gives a chance to detect only the solution of RI difference. A linear output power and temperature relation is obtained fitting with the negative thermo-optic coefficient variation.

To understand polishing depth effect on response for temperature, the sensitivity of sensors is calculated and presented in Table 5.2. The results agree with the Table 5.1 for the first zone. There is no solution between 1.44 and 1.47 RIs. The sensitivity to

the temperature increases with increasing polishing depth except -20 μm deep sensor by reason of high loss on the output power.

Table 5.2 Sensitivities for sensors with different polishing depths at different temperatures.

Wavelength	Temperature range	Bio-layer RI	Polishing Depth, $h(\mu\text{m})$	Sensitivity ($\delta P_{\text{norm}}/\delta T$)
633 nm	23 °C - 30 °C	$n = 1.43$ at 25 °C	+5	83.3
			-5	64.1
			-10	25.5
			-20	268.8

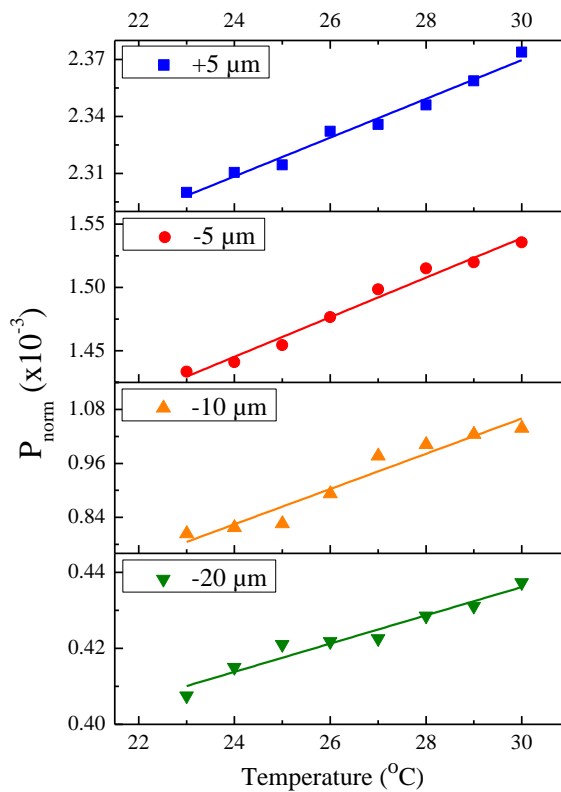


Figure 5.5 The temperature effect on the sensor's response.

5.4 Results of Surface Modification

Total reflection of different thickness gold-layer deposited D-type F/O sensors are examined analytically for the range of refractive indices between 1.33 and 1.47. The output powers are determined by running the WinSpall™ software which utilizes Fresnel equations. The model consists of 4 layers; fiber core, Cr film, gold film, and bio-layer. Calculations depend on the configurations of infinite thickness fiber core; 2 nm Cr film; and 0 nm - 30 nm thin gold films. In fact, computed results are used to analyze optical multilayer sensor systems. The results in Figure 5.6 (a) are the total reflection graph of the 20 nm gold layer coated sensor for varying refractive indices between 1.33 and 1.47.

The surface plasmon resonance (SPR) mode is observed that as the thickness of gold film is increased from 10 nm to 30 nm, the resonance point shifts to the left from 1.43 to 1.35. The shown resonance points with respect to the combination of surrounding medium refractive index ($n_{surr.}$) and thickness of gold film (t_{gold}) is demonstrated in Figure 5.6 (b). On the other hand, Figure 5.6 (c) presents difference on resonance angle shifts by determining the gold thickness and biolayerRI. If the absolute value of the difference on resonance angle shift is higher, the sensor response around that point is better. In the same figure, the highest shift zone is marked with a dotted line. It is observed that sensors' responses between 1.33 and 1.47 are not linear for a given gold layer thickness. Furthermore, the black zone shown in Figure 5.6 (c) does not give any solution that has physical meaning. Moreover, it is not possible to get any model result in this region.

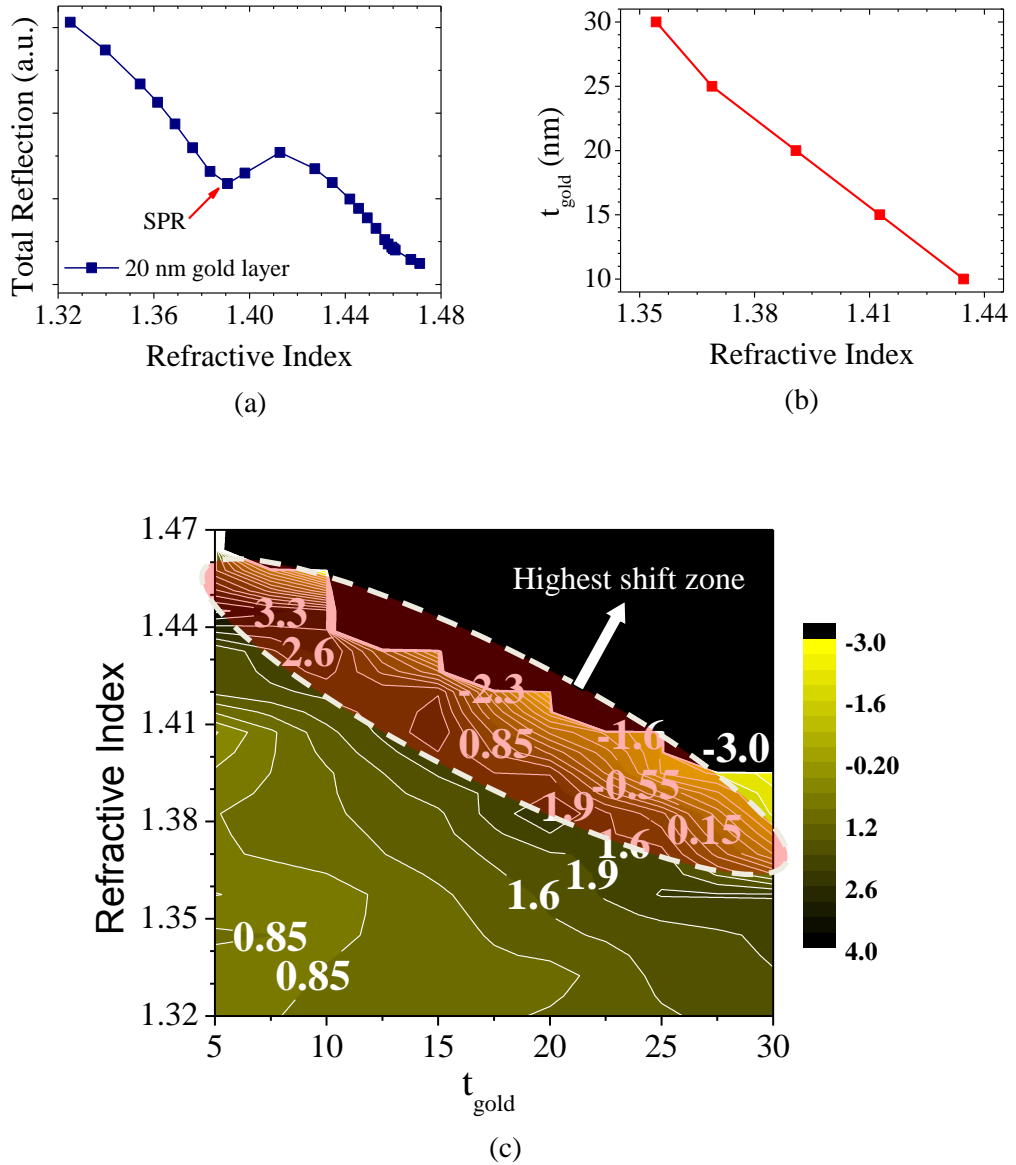


Figure 5.6 (a) Simulation results for 20 nm Au & 2 nm Cr coated sensors, (b) resonance points for different gold-layer thicknesses (30-25-20-15-10-0 nm Au) – RI combinations, (c) Angular shift as functions of t_{gold} and n_{surr} .

5.4.1 F/O sensors with SPR and OWG Modes

In order to excite surface plasmon resonance and waveguide (SPR+OWG) modes, the 5 mm-long section of the -5 μm and the -20 μm deep polished sensors are coated with 20 nm-thickness gold films. Both the output and the input powers with respect to varying the refractive indices between 1.33-1.47 are measured. Normalized forms of measured power for sensors are illustrated in Figure 5.7 (a) and (b). For -5 μm

deep polished sensor, two resonance points are observed due to the existence of both SPR and OWG modes (Figure 5.7 (a)). While OWG mode gives a narrow and sharp resonance at the RI = 1.44, SPR mode indicates a broader resonance. On the other hand, when gold coated -5 μm and -20 μm deep polished sensors are compared, the SPR point shifts slightly to right to higher RI and the OWG mode disappears. The broad SPR mode becomes narrower and sharper for -20 μm deep polished sensors. Additionally, approaching the bio-layer RI to the fiber core RI decreases the gold film effect on sensor response for both gold coated sensors. That is, there is only waveguide modes existence between 1.44 and 1.47 ranges. Also, the simulation results in Figure 5.6 (c) supports that solutions are not take place for refractive indices between 1.44 and 1.47.

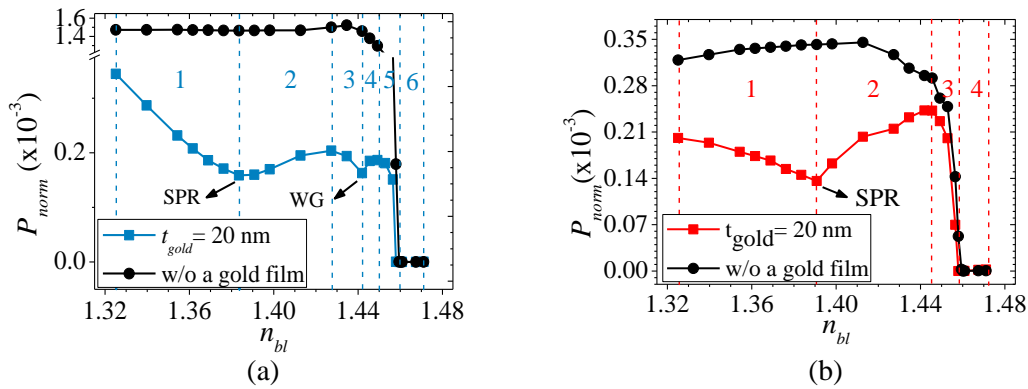


Figure 5.7 Normalized power results a function of RI for (a) -5 μm and (b) -20 μm deep polished with SPR+OWG sensors.

The D-type SPR F/O sensor performance can be defined with a sensitivity parameter that is the indication of how good sensor's response to the less amount of molecular concentrations. We use $\delta P_{\text{norm}}/\delta n$ term ($1/\text{RIU}$) as the sensitivity. To calculate the sensitivities of sensors, different RI zones are defined according to measured data for shown in Figure 5.7 (a) and (b). The calculated sensitivities of -5 μm and the -20 μm deep polished sensors with and without gold layer are given in Table 5.3. For the -5 μm deep polished sensor, gold coating increases the sensitivity of sensor between the refractive indices 1.33-1.44 and 1.46-1.47. Generally, higher sensitivities are

obtained except the 2nd zone (1.3835-1.4273). In fact, the existence of OWG mode at 1.44 and the broadened SPR mode decreases the 2nd zone sensitivity of the sensor.

Table 5.3. Sensitivities for OWG and OWG+SPR type F/O sensors at different polishing deep and RI zones.

Wavelength	Temperature	Polishing Depth, h (μm)	Sensor Modes	Zone	RI	Sensitivity ($\delta P_{\text{norm}}/\delta n$) (1/RIU)
633 nm	25°C	-5	OWG	1	1.3251 - 1.4419	1095.3
				2	1.4419 - 1.4601	187265.9
				3	1.4601 - 1.4711	26.4
			OWG+SPR	1	1.3251-1.3835	7142.8
				2	1.3835-1.4273	2331.0
				3	1.4273-1.4419	6289.3
		4		1.4419-1.4492	7246.3	
		5		1.4492-1.4594	40983.6	
		6		1.4594-1.4711	55.5	
		-20	OWG	1	1.3251 - 1.4419	471.7
				2	1.4419 - 1.4601	37878.8
				3	1.4601 - 1.4711	6.3
			OWG+SPR	1	1.3251-1.3908	2232.1
				2	1.3908-1.4455	4405.3
				3	1.4455-1.4580	44052.9
				4	1.4580-1.4711	395.3

Furthermore, the sensor sensitivity decreases for the RI 1.44 and 1.46 with gold layer deposition. Light absorbance of gold layer affects the sensor sensitivity negatively for the 1.44-1.46. The sensitivity of the -20 μm deep polished sensor is increased with gold layer coating for the RI ranges between 1.44 and 1.47. The highest sensitivity is observed at the 3rd zone (1.4455-1.4580). Also, a dramatic sensitivity increase derived for the 1st and 2nd zones (1.3251- 1.4455).

5.4.2 Roughened F/O Sensor

To study the influence of surface roughness and increase the sensitivity of sensor between the RI ranges 1.33-1.40, plasma etching is applied onto the surface of the -5 μm polished and gold coated sensor. The increasing plasma etching time results in a decreasing gold film thickness and increasing surface roughness. The measured roughness values are 3.0 nm, 5.6 nm, and 7.8 nm for 0, 2, and 4 minutes plasma etchings respectively as presented in Figure 5.8. The resonance point shifts to higher refractive indices and the OWG mode disappears so the sensor sensitivity changes for zones as demonstrated in Figure 5.8. In fact, slightly increasing roughness provides higher sensitivity due to the increased interaction length and scattering effect of the rough surface. In table 5.4, sensitivities of sensor are given. The obtained highest sensitivity is obtained with the 2 min-plasma etching applied sensor. The acquired sensitivity between 1.3251-1.3981 refractive indices is 8403.3 1/RIU. However, applying plasma etching too much decreases both the gold film thickness and the sensor sensitivity.

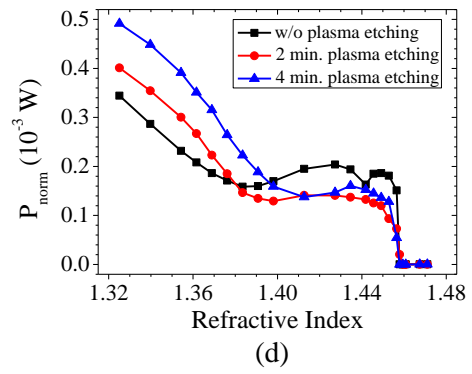
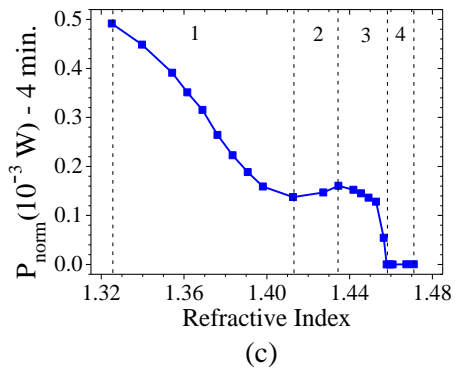
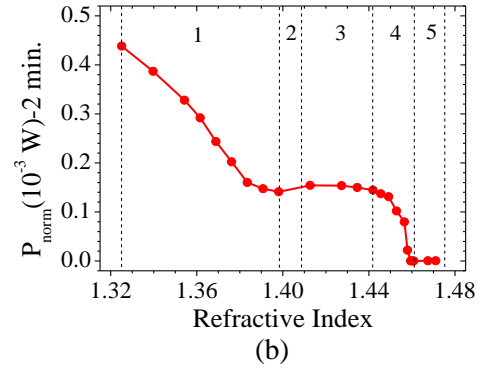
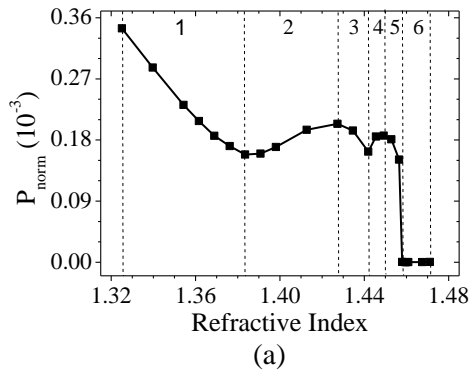


Figure 5.8 Results of a) 0 min. b) 2 min. c) 4 min. d) 0-2-4 min. plasma etching applied to the $-5 \mu\text{m}$ deep polished sensor.

Table 5.4 Plasma etching applied -5 polishing depth SPR sensor sensitivities for different zones.

Wavelength	Temperature	Polishing Depth (h μm)	Plasma Etching Time	Zone	RI	Sensitivity ($\delta P_{\text{norm}}/\delta n$) (1/RIU)
633 nm	25 °C	-5	0 min.	1	1.3251-1.3835	7142.9
				2	1.3835-1.4273	2331.0
				3	1.4273-1.4419	6289.3
				4	1.4419-1.4492	7246.4
				5	1.4492-1.4594	40983.6
				6	1.4594-1.4711	55.6
			2 min.	1	1.3251-1.3981	8403.3
				2	1.3981-1.4273	892.9
				3	1.4273-1.4492	2123.1
				4	1.4492-1.4609	24813.9
				5	1.4609-1.4711	58.8
			4 min.	1	1.3251-1.4127	8333.3
				2	1.4127-1.4346	2188.2
				3	1.4346-1.46088	12626.3
				4	1.46088-1.4711	80.0

5.5 Biological Measurements

In this section, it is demonstrated that the real-time molecular interaction is possible with the developed D-type F/O sensors. IgG proteins are detected with the -5 μm deep polished, 20 nm thick gold film coated, and 2 min. RF plasma etched F/O sensor. Rabbit Anti-Mouse IgG (RAM) is used as the antibody reagent, while Mouse IgG (MIgG) protein is selected as the antigen reagent. The 10 $\mu\text{g}/\mu\text{L}$ RAM and 50 $\mu\text{g}/\mu\text{L}$ MIgG mixtures are prepared inside Phosphate Buffered Saline (PBS) and they are syringed into the flow cell respectively. In Figure 5.9, the output power change as a function of the time is presented for the IgG molecular interactions. The obtained data in measurements are smoothed by using signal processing Savitzky-Golay method.

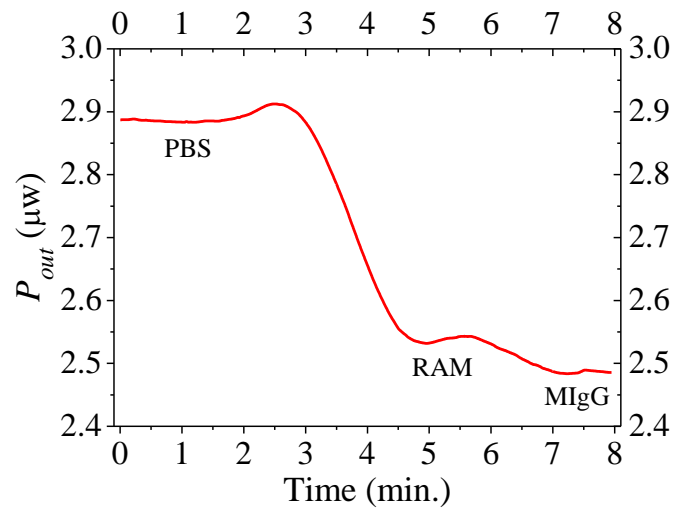


Figure 5.9 Detection of IgG molecules as a function of the output power.

CHAPTER 6

CONCLUSIONS

The aim of this study is to develop D-type F/O sensors for biological measurements. These type sensors have many advantages such as being repeatable and reusable, presenting high level of miniaturization and having real-time detection. Long-flat surface of D-type F/O sensors make them more sensitive for detecting molecular interaction at low concentrations. In fact, they can analyze intricate molecular interactions in aqueous environments with measuring the variations in RI. The D-type multimode F/O sensors with the 25 mm-long-interaction length have been fabricated. Evanescent field in the core section of the F/O cable was exposed to bio-layer by mechanical polishing process to understand sensor's response in different RI regions. Also effects of critical parameters such as the polishing depth, the wavelength, and the temperature on sensors' output are studied for RI sensing between 1.33 and 1.47.

Various sensitivities are observed in three different RI zones (I: 1.32-1.44, II: 1.44-1.46, III: 1.46-1.47). The polishing depth effects on these zones are studied at fix wavelengths and the temperature. The maximum measured sensitivity for the +5 μm sensor shows that it is capable of detecting changes in the refractive indices between 1.44 and 1.46 with a sensitivity of $\sim 2 \times 10^{-5}$. However, this sensitivity is not enough for measuring small changes in biological suspensions such as bio-mixtures or bio-films of proteins, DNA, antibodies, cell surface receptors, peptides, organic molecules, oligonucleotides in liquids such as phosphate buffered saline (PBS),

blood plasma, hemoglobin solution, lecithin and cholesterol mixtures. Such biological medium may have a complex RI ($m = n + ik$) and its real part (n) may vary between 1.33 and 1.39. This RI region sensitivity can be increased with generating SPR mode. Therefore, D-type evanescent wave F/O sensors with the 5 mm-long-gold coated section are fabricated at different polishing depths and surface roughness. The modifications on sensor's structure and deposition of thin gold layer make both SPR and OWG modes to be excited at the same time. Adjusting polishing depth and surface roughness with decreasing gold thin film layer can improve the sensitivity of sensors for different RI range zones between 1.33 and 1.39.

Enhancing performance of the sensor response is possible with expending this study. Some of suggestions/improvements for future work are listed as follows:

- Improvements on lapping-polishing procedure to get better and flat sensor's surfaces can increase sensitivity of sensor.
- Upgrading components of the optical system. A stable laser can improve signal to noise ratio for measurements. Better detectors to decrease its minimum reading signal. Better light coupling into F/O cable decreases the losses.
- The sensor's sensitivity for a required dynamic range may be increased with changing length and thickness of the metal layer by combining an appropriate roughness of the surface.
- Surface can be functionalized for different biological molecular interaction measurements.
- Development more compact and multichannel F/O sensor arrays can provide different molecular measurements simultaneously.

REFERENCES

- 1 Saleh B. E. A., Telch M. C., Fundamentals of Photonics John Wiley & Sons, inc., 1991, pp 249–292.
- 2 Fan X., White, M. I., Sun I., Sensitive optical biosensors for unlabeled targets: A review. *Analytica Chimica Acta*, 2008, 620, 8-26.
- 3 Lin H. Y., Tsai W. H., Sheu C. B., Side-polished multimode fiber biosensor based on surface plasmon resonance with halogen light. *Applied Optics*, 2007, 46, 800-806.
- 4 Yanase Y. Araki A., Hide M., Development of an optical fiber SPR sensor for living cell activation. *Biosensors and Bioelectronics*, 2010, 25, 1244–1247.
- 5 Liu X., Tan W., A Fiber-Optic Evanescent Wave DNA Biosensor Based on Novel Molecular Beacons. *Analytic Chemistry*, 1999, 71, 5054-5059.
- 6 Homola J., Surface Plasmon Resonance Sensors for Detection of Chemical and Biological Species. *Chemical Review*, 2008,108, 462-493.
- 7 Ligler F. S., C. R. Taitt, Optical Biosensors: Today and Tomorrow, Elsevier B. V., 2nd edition 2008, pp. 83-145.
- 8 X. Liu, D, Song, H. Zhang, Wavelength-modulation surface plasmon resonance sensor. *Trends in Anal. Chem.*, 2005, 24, 887-893.
- 9 Leung A., Shankar M. P., Mutharasan R., A review of fiber-optic biosensors. *Sensors and Actuators B*, 2007, 125, 688–703.
- 10 Yin S., Zhan C., Ruffin P. B., Fiber Optic Sensors, Second Edition, CRC Press, 2008, pp 436-455.
- 11 Méndez A., Morse T. F., Specialty Optical Fibers Handbook, Elsevier, 2007, pp 20-65.
- 12 Hunsperger R. G., Integrated Optics – Theory and Technology, Springer, 6th edition, 2009, pp 33-49.

- 13 Sharma K. A., Jha R., Gupta B. D., Fiber-Optic Sensors Based on Surface Plasmon Resonance: A Comprehensive Review. *IEEE Sensors Journal*, 2007, 7, 1118-1129.
- 14 Tseng S. M., Chen L. C., Side-polished fibers. *Applied Optics*, 1992, 31, 3438-3447.
- 15 Chen C. H., Chao T. Z., Li W. Y., Chau K. L., Novel D-type Fiber Optic Localized Plasmon Resonance Sensor Realized by Femtosecond Laser Engraving. *Journal of Laser Micro/Nanoengineering*, 2010, 5, 1-5.
- 16 Lee H., Kim H., Park H. J., Jeong J. H., Lee S. K., Effects of surface density and size of gold nanoparticles in a fiber-optic localized surface plasmon resonance sensor and its application to peptide detection. *Measurement Science and Technology*, 2010, 21, 1-9.
- 17 Villuenda F., Pelayo J., Optical Fibre Device for Chemical Sensing Based on Surface Plasmon Excitation. *Sensors and Actuators A21-A23*1990, 1142-1145.
- 18 Jorgenson R. C., Yee S. S., A fiber-optic chemical sensor based on surface plasmon resonance. *Sensors and Actuators B*, 1993, 12, 213-220.
- 19 Gupta B. D., Verma R. K., Surface Plasmon Resonance-Based Fiber Optic Sensors: Principle, Probe Designs, and Some Applications. *Journal of Sensors*, 2009, DOI: 10.1155/2009/979761.
- 20 Ahmad M., Hench L. L., Effect of taper geometries and launch angle on evanescent wave penetration depth in optical fibers. *Biosensors and Bioelectronics*, 2005, 20, 1312-1319.
- 21 Andreev A. T., Zafirova S. B., Karakoleva E. I., Single-mode fiber polished into the core as a sensor element. *Sensors and Actuators A*, 1998, 64, 209-212.
- 22 Srivastava S. K., Verma R., Gupta B. D., Surface plasmon resonance based fiber optic sensor for the detection of low water content in ethanol. *Sensors and Actuators B*, 2011, 153, 194-198.
- 23 Slavík R., Homola J., Čtyroký J., Single-mode optical fiber surface plasmon resonance sensor. *Sensors and Actuators B*, 1999, 54, 74-79.
- 24 Dwivedi S. Y., Sharma A. K., Gupta A. K., Influence of Design Parameters on the Performance of a Surface Plasmon Sensor Based Fiber Optic Sensor. *Plasmonics*, 2008, 3, 79-86.
- 25 Zhou W., Shen H. P., Pamulapati J., Optical Waveguide Components, *Encyclopedia of Electrics and Electronic Engineering*, 1st edition, 1999, 339-354.

- 26 Wang X. D., Wolfbeis O. S., Fiber-Optic Chemical Sensors and Biosensors (2008–2012). *Analytical Chemistry* 2013, 85, 487-508.
- 27 Knoll W., Interfaces and thin films as seen by bound electromagnetic waves. *Annu. Rev. Phys. Chem.*, 1998, 49, 569–638.
- 28 Träger, F., Handbook Lasers and Optics, Springer, 2nd edition, 2012, pp 253-400.
- 29 Harris R. D., Wilkinson J. S., Waveguide surface plasmon resonance sensors. *Sensors and Actuators B*, 1995, 29, 261-267.
- 30 Horvath R., Pedersen H. C., Skivesen N., Optical waveguide sensor for on-line monitoring of bacteria. *Optics Letters*, 2003, 28, 1233-1235.
- 31 Qi M. Z., Itoh K., Murabayashi M., Characterization and application of a channel-planar composite waveguide. *Optics Letter*, 2000, 25 (19), 1427-1429.
- 32 Dostálek J., Čtyroký J., Homola J., Brynda E., Schröfel J., Surface plasmon resonance biosensor based on integrated optical waveguide. *Sensors and Actuators B*, 2001, 76, 8-12.
- 33 Špačková B., Piliarik M., Kvasnička P., Homola J., Novel concept of multi-channel fiber optic surface plasmon resonance sensor. *Sensors and Actuators B*, 2009, 139, 199–203.
- 34 Long F., Gao C., Shi H. C., Gu A. Z., Reusable evanescent wave DNA biosensor for rapid, highly sensitive, and selective detection of mercury ions. *Biosensors and Bioelectronics*, 2011, 26, 4018–4023.
- 35 Masson J. F., Obando L., Beaudoin S., Booksh K., Sensitive and real-time fiber-optic-based surface plasmon resonance sensors for myoglobin and cardiac troponin I. *Talanta*, 2004, 62, 865–870.
- 36 Mukundan H., Anderson A. S., Waveguide-Based Biosensors for Pathogen Detection. *Sensors*, 2009, 9, 5783-5808.
- 37 Yeh C., Shimabukuro F., The Essence of Dielectric Waveguides, Springer, 2008, pp. 99-135.
- 38 Okamoto K., Fundamentals of Optical Waveguides, Academic Press, 2nd edition, 2006, pp. 13-54.
- 39 Lukosz W., Integrated optical chemical and direct biochemical sensors. *Sensors and Actuators B*, 1995, 29, 37-50.

- 40 Mouvet C., Harris R. D., Wilkson J. S., Determination of simazine in water samples by waveguide surface plasmon resonance. *Analytica Chimica Acta*, 1997, 338, 109-117.
- 41 Eric U., *Fiber Optic Sensors - An Introduction for Engineers and Scientists*, Wiley-Interscience, 2006, pp. 9-36/ 407-439.
- 42 Bilro L., Alberto N. J., Nogueira R., Analytic Analysis of Side-Polished Plastic Optical Fiber as Curvature and Refractive index Sensor. *Journal of Lightwave Technology*, 2011, 29, 864-870.
- 43 Cheng F. S., Chau L. K., Colloidal Gold-Modified Optical Fiber for Chemical and Biochemical Sensing. *Anal. Chem.*, 2003, 75, 16-21.
- 44 Schmitt, Ron, *Electromagnetics Explained A Handbook for Wireless/ RF, EMC, and High-Speed Electronics*, Elsevier, 2002, pp 181-207.
- 45 Navarrete M. C., Herrera N. D., A Polarization-Independent SPR Fiber Sensor. *Plasmonics*, 2010, 5, 7-12.
- 46 Lee B., Roh S., Park J., Current status of micro- and nano-structured optical fiber sensors. *Optical Fiber Technology*, 2009, 15, 209–221.
- 47 Diez A., Andres M. V., Cruz J. L., In-line fiber-optic sensors based on the excitation of surface plasma modes in metal-coated tapered fibers. *Sensors and Actuators B*, 2001, 73, 95-99.
- 48 Jha R., Gupta B. D., Surface Plasmon Resonance-Based Tapered Fiber Optic Sensor: Sensitivity Enhancement by Introducing a Teflon Layer Between Core and Metal Layer. *Plasmonics*, 2008, 3, 151–156.
- 49 Villatoro J., Fabrication and modeling of uniform-waist single-mode tapered optical fiber sensors. *Applied Optics*, 2003, 42, 194-198.
- 50 Srivastava S. K., Surface plasmon resonance based fiber optic sensor for the detection of low water content in ethanol. *Sensors and Actuators B*, 2011, 153, 194–198.
- 51 Mishra K. S., Kumari D., Gupta B. D., Surface plasmon resonance based fiber optic ammonia gas sensor using ITO and polyaniline. *Sensors and Actuators B*, 2012, 161, 976– 983.
- 52 Bhatia P., Gupta D. B., Surface plasmon resonance based fiber optic refractive index sensor utilizing silicon layer: Effect of doping . *Optics Communications*, 2013, 286, 171–175.

- 53 Chang Y. J., Chen Y. C., Kuo H. L., Wei P. K., Nanofiber optic sensor based on the excitation of surface plasmon wave near fiber tip. *Journal of Biomedical Optics*, 2006, 11 (01), 014032.
- 54 Suzuki H., Sugimoto M., Matsui Y., Kondoh J., Effects of gold film thickness on spectrum profile and sensitivity of a multimode-optical-fiber SPR sensor. *Sensors and Actuators B*, 2008, 132, 26–33.
- 55 Lin Y., Zou Y., Mo Y., Guo J., Lindquist R. G., E-Beam Patterned Gold Nanodot Arrays on Optical Fiber Tips for Localized Surface Plasmon Resonance Biochemical Sensing. *Sensors*, 2010, 10, 9398-9406.
- 56 Chau L. K., Lin Y. F., Cheng S. F., Lin T. J., Fiber-optic chemical and biochemical probes based on localized surface plasmon resonance. *Sensors and Actuators B*, 2006, 113, 100–105.
- 57 Piliarik M., Homola J., Manikova Z., Čtyroký J., Surface plasmon resonance sensor based on a single-mode polarization-maintaining optical fiber. *Sensors and Actuators B*, 2003, 90, 236–242.
- 58 Slavik R., Homola J., Čtyroký J., Brynda J., Novel spectral fiber optic sensor based on surface plasmon resonance. *Sensors and Actuators B*, 2001, 74, 106-111.
- 59 Beam B. M., Waveguide sensor platforms: a) development of the electroactive fiber- optic chip and b) attenuated total reflectance spectroscopy of new molecular materials, The University of Arizona, Doctorate Thesis, 2008.
- 60 Bhatia P., Gupta B. D., Fabrication and characterization of a surface plasmon resonance based fiber optic urea sensor for biomedical applications. *Sensors and Actuators B*, 2012, 161, 434– 438.
- 61 Fishbane P. M., Gasiorowics G. S., Thornton S. T., Physics for Scientist and Engineers with Modern Physics, Pearson Education Inc., 3rd edition, 2005, pp. 943-991.
- 62 Griffiths D. J., Introduction to electrodynamics, Pearson Education Inc., 3rd edition, 2008, pp 321-345.
- 63 Pedrotti L. F., Pedrotti M. L., Pedrotti L. S., Introduction to Optics, Pearson Education Inc., third edition, 2008, pp. 8-9.
- 64 California Institute of Technology (Project Scientist: C. R. Lawrence), The electromagnetic spectrum can be found under <http://planck.caltech.edu>, 2013, [Last Accessed on 27/06/2014].

- 65 Čtyroký J., Homola J., Skalský M., Modelling of surface plasmon resonance waveguide sensor by complex mode expansion and propagation method. *Optical and Quantum Electronics*, 1997, 29, 301-311.
- 66 Lukosz W., Principles and sensitivities of integrated optical and surface plasmon sensors for direct affinity sensing and immunosensing. *Biosensors & Bioelectronics*, 1991, 6, 215-225.
- 67 Singh S., Verma R. K., Gupta B. D., LED based fiber optic surface plasmon resonance sensor. *Optical Quantum Electronics*, 2010, 42, 15–28.
- 68 Vanderlinde J., Classical Electromagnetic Theory, Kluwer Academic Publishers, 2nd edition, 2005, pp 243-276.
- 69 Ma J., J. Bock W., Dramatic performance enhancement of evanescent-wave multimode fiber fluorometer using non-Lambertian light diffuser. *Optics Express*, 2007, 15, 16457- 16470.
- 70 Petersen K. E., Silicon as a mechanical Material. *Proceedings of the IEEE*, 1982, 70 (5), 420-457.
- 71 Groover M. P., Fundamentals of modern manufacturing: materials, processes, and systems, Jhon Wiley & Sons, Inc, 3rd edition, 2007, pp. 798-825.
- 72 Lin J. B., Optical Lithography: Here is Why, SPIE Bellingham, Washington, 2010, pp 1-200.
- 73 Campbell S. A., The Science and Engineering of Microelectronic Fabrication, Oxford University Press, Oxford, New York, 2nd edition, 2001, pp 151-196.
- 74 Nijdam A. J., Berenschot J. W., Suchtelen J. V., Elwenspoek M., Velocity sources as an explanation forexperimentally observed variations in Si (111) etch rates. *Journal of Micromech. Microengineering*, 1999, 9, 135-138.
- 75 Yun M. H., Burrows V. A., Kozicki M. N., Analysis of KOH etching of (100) silicon on insulator for the fabrication of nanoscale tips. *J. Vac. Sci. Technol. B*, 1998, 16 (5), 2844-2848.
- 76 Seidel H., Csepregi L., Baumgartel H., Anisotropic Etching of crystalline Silicon in Alkaline Solutions. *J. Electrochem. Soc.*, 1990, 137, 3612-3626.
- 77 Hertl W., Hair M. L., Reaction of Hexamethyldisilazane with Silica. *The Journal of Physical Chemistry*, 1971, 76 (14), 2181-2185.
- 78 Zubel I., Kramkowska M., The effect of isopropyl alcohol on etching rate and roughness of (100) Si surface etched in KOH and TMAH solutions. *Sensors and Actuators A*, 2001, 93, 138-147.

- 79 Marinescu I. D., Uhlmann E., Doi T., Handbook of Lapping and Polishing, CRC Press, Taylor&Francis Group, US, 2007, pp 1-5.
- 80 Martin M. P., Handbook of deposition technologies for films and coatings: science, applications and technology, Plenum Press, New York, 3rd edition, 2009, pp 2-10.
- 81 Haes, A. M., Haynes, C. L., Duyne, R. P. V., Nanosphere Lithography: Self-Assembled Photonic and Magnetic Materials, *Mat. Res. Soc. Symp.*, 636, 2001.